Stretch and flow at the gliovascular interface: high-fidelity modelling of the mechanics of astrocyte endfeet

Marius Causemann[1], **Rune Enger**[2,3,4], **and Marie E. Rognes**[1,4,*]

[1]Department of Numerical Analysis and Scientific Computing, Simula Research Laboratory, Kristian Augusts gate 23, 0164 Oslo, Norway
[2]Institute of Basic Medical Sciences, University of Oslo, Oslo, Norway
[3]Department of Neurosurgery, Oslo University Hospital - Rikshospitalet, Oslo, Norway
[4]K. G. Jebsen Centre for Brain Fluid Research, Oslo, Norway
[*]meg@simula.no

ABSTRACT

Astrocyte endfeet form a near-continuous sheath around the brain's vasculature, defining the perivascular space (PVS) implicated in fluid flow and solute transport. Yet, their precise physiological role remains incompletely understood. This study combines electron microscopy data with a high-fidelity poroelastic computational model to investigate the mechanical interplay at the gliovascular interface. We simulated tissue displacement and fluid flow within detailed reconstructions of the PVS, endfeet, and extracellular space (ECS) in response to cardiac-induced arteriole pulsations. Our model predicts that arteriole dilation compresses the PVS while expanding the overall endfoot sheath volume due to tangential stretch. Fluid exchange primarily occurs through inter-endfoot gaps, driven by pressure differences, rather than across the aquaporin-4 (AQP4) rich endfoot membrane. PVS stiffness critically modulates these dynamics: increased stiffness can reverse PVS volume changes and flow directionality, potentially minimizing fluid exchange at intermediate stiffness levels. While AQP4 has negligible impact on pulsation-driven mechanics, it significantly enhances osmotically driven fluid flow. These findings highlight the complex balance of forces governing gliovascular mechanics and suggest PVS composition strongly influences endfoot-parenchymal fluid exchange.

Introduction

Astrocytes, the main macroglial cell of grey matter, have exceedingly complex morphology. In addition to tiny cellular protrusions that fill the gaps between the other constituents of the neuropil, astrocytes form a sheath around the brain's vasculature, the glia limitans perivascularis, by endfoot processes extending from the soma towards the vessel, or by residing juxtavascularly [Grubb, 2023]. Thus, endfeet form a nearly continuous barrier layer around the brain's vasculature [Grubb, 2023, Mathiisen et al., 2010] and hence define the outer perimeter of the perivascular spaces (PVS). However, the precise role of astrocyte endfeet remains enigmatic. In some sharks and other elasmobranches, the endfoot sheath is believed to be the main constituent of the blood-brain barrier [Abbott et al., 1986], whereas in mammals, there are likely gaps between neighbouring endfoot processes, hindering the endfeet from acting as a tight barrier. Endfoot signaling has been suggested to play a role in blood flow control [Gordon et al., 2007, MacVicar and Newman, 2015], but these mechanisms remain controversial.

Cerebrospinal fluid (CSF) flow in the PVS likely plays a key role in brain waste clearance through the so-called glymphatic system [Iliff et al., 2012]. In this system, the PVS allow the CSF to efficiently distribute through the brain, exit into the tissue, mix with the interstitial fluid, and in the process clear out extracellular waste products, such as beta-amyloid. These mechanisms were also shown to be considerably more effective in sleep [Xie et al., 2013]. Since the glymphatic system plays a role in the removal of extracellular waste products, it is considered a physiological mechanism preventing neurodegenerative disease. This concept serves as an extension of work by Helen Cserr and colleagues, demonstrating that PVS enable faster-than-diffusion movement of solutes throughout the brain [Cserr and Ostrach, 1974, Ichimura et al., 1991]. Although passive vessel pulsations from the heartbeat and respiration as well as active vascular dynamics likely are the main drivers of this extracellular waste clearance system, the mechanical forces and interactions between the blood vessels, the surrounding PVS and the astrocytic endfeet remain only rudimentarily understood.

Recent evidence highlights that the composition of the PVS is heterogeneous between different vessels and may change with ageing and vessel pathology [Mestre et al., 2022]. Crucially, changes in the PVS' composition of extracellular matrix proteins, associated with ageing and Alzheimer's disease and potentially involving dysfunctional perivascular macrophages,

have been proposed to affect both vessel dynamics and perivascular fluid dynamics [Drieu et al., 2022]. It is beyond existing experimental approaches to probe how altered PVS composition affects mechanical coupling between the vessel, PVS and endfeet. Moreover, nearly 50% of the surface area of the endfeet facing the vasculature is covered by aquaporin-4 (AQP4) water channels. AQP4 is a passive, bi-directional transmembrane water channel, a tetramer that can form supramolecular structures in the form of so-called orthogonal arrays of particles [Nagelhus and Ottersen, 2013]. In the brain, AQP4 has been extensively studied in the context of pathophysiology, in particular in brain edema. Here, removal of aquaporin-4 may be protective for certain types of edema formation, but detrimental for other types of edema. Further, AQP4 expression patterns are known to be disrupted in a range of brain disorders, both when studied in animal disease models, or in patient tissue [Nagelhus and Ottersen, 2013]. The role of AQP4 in physiology, however, is less clear.

Mechanical forces are ubiquitous in neurobiological processes, influencing cellular mechanisms such as neuron growth, synapse formation, and brain tissue development and clearance [Pillai and Franze, 2024, Tyler, 2012]. These forces, including fluid flow, mechanical stress, and tissue deformation, are integral to understanding how physical interactions can affect brain function and pathology. Despite their importance, measuring these forces at the cellular level presents significant challenges. Electron microscopy (EM) provides high spatial resolution, but introduces significant artifacts and, as a post-mortem method, is inherently unable to capture the functional dynamics in living brain tissue. In contrast, traditional in vivo imaging techniques such as two-photon microscopy often lack the resolution required to capture the dynamics of mechanical forces within the brain's complex microenvironment, with water movement on the microscopic scale being exceedingly difficult to assess experimentally. Computational modelling emerges as a powerful tool to overcome these challenges, offering a non-invasive approach to simulate and analyze the biomechanical interactions of neural and glial cells, extracellular matrix and the cerebral vasculature. By harnessing structural imaging techniques, high-performance computing and novel modelling approaches, computational models can provide insights into the impact of mechanical forces on cellular behaviour, helping to shed light on complex physiological processes that are otherwise impossible to measure directly.

In this study, we combine electron microscopy imaging data with a poroelastic modelling approach to introduce a high-fidelity computational model of the mechanical interplay at the gliovascular interface. Focusing on cardiac-induced arteriole pulsations, our model predicted the temporospatial evolution of tissue displacement and fluid flow in a detailed geometric representation of PVS, endfeet and ECS. We find that arteriole dilation induces endfoot sheath expansion, and drives fluid into the surrounding neuropil, but through the endfoot gaps rather than across the endfoot membrane. These oscillatory pressure and fluid flow patterns are governed by a complex balance of radial compression and tangential stretch of the structures involved, suggesting that the PVS composition of extracellular matrix and cells may strongly affect gliovascular dynamics and endfoot–parenchymal fluid exchange. In particular, we find that PVS stiffening reverse the PVS volume, pressure and flow dynamics across the cardiac cycle, with minimal fluid exchange at certain PVS stiffnesses.

Results

Digital high-resolution reconstruction and representation of the astrocyte endfoot sheath

The gliovascular unit, formed by astrocytes and astrocytic endfeet, ensheathing vascular and perivascular spaces, dynamically and rhythmically moves in response to changes in its environment (Figure 1A-B). In order to create a high-fidelity in-silico platform for predicting the mechanical response of this fundamental structure, we turned to a high-resolution segmentation of the extravascular surroundings of an arteriole in the mouse visual cortex [Turner et al., 2022] (Figure 1C). Along a 20 µm-segment of this vessel, we identified six astrocyte endfeet, together ensheathing a PVS surrounding the vessel lumen. Using the fTetWild meshing software [Hu et al., 2020], we created a conforming tessellated representation of the individual endfeet, the PVS, and the remaining (non-PVS) ECS (Figure 1D-E), while compensating for artifacts from chemical fixation (see Methods). The mean arteriole diameter of 12.2 µm and mean PVS width of 4.6 µm resulted in a mean inner endfoot sheath diameter of 16.8 µm and an outer diameter of 21.0 µm (Figure 1F). In terms of volume, the PVS occupied 41% of the reconstructed geometry, while each endfoot occupied between 0.4 and 9%, giving a total of 30% for all endfoot fragments combined (Figure 1G). With an additional 19% for other neuronal and glial cells next to the endfeet, the ECS occupied the remaining 10%, which translates to an extracellular volume share of 16.6% of the endfoot sheath alone (disregarding the PVS). Characterizing the shape and width of the ECS, we observed a heterogeneous geometry, with tight inter-endfeet gaps and channels (10–50 nm), most spaces ranging between 20 and 120 nm, but also some larger pools up to 500 nm wide (Figure 1H).

We then represented the spatially-resolved astrocyte endfeet and other neural and glial cells, the PVS and the ECS as separate domains and considered each as deformable and permeable (poroelastic) structures, separated by the semi-permeable cell membranes. We set the stiffness and (in)compressibility of the astrocyte endfoot skeleton to be 10× that of the ECS and PVS, and the permeability of the PVS to be 10× that of the ECS, which in turn is set twice that of the astrocyte endfeet. Crucially, we also distinguished between the permeability of the AQP4-rich adluminal endfoot membrane and the abluminal side (see Methods). The mechanical response of this environment is then described by the displacement field $\mathbf{d}$ and the fluid pressure field p, with the fluid flux $\mathbf{q}$ and stress tensor $\boldsymbol{\sigma}$ as auxiliary derived fields, all varying across space and time.

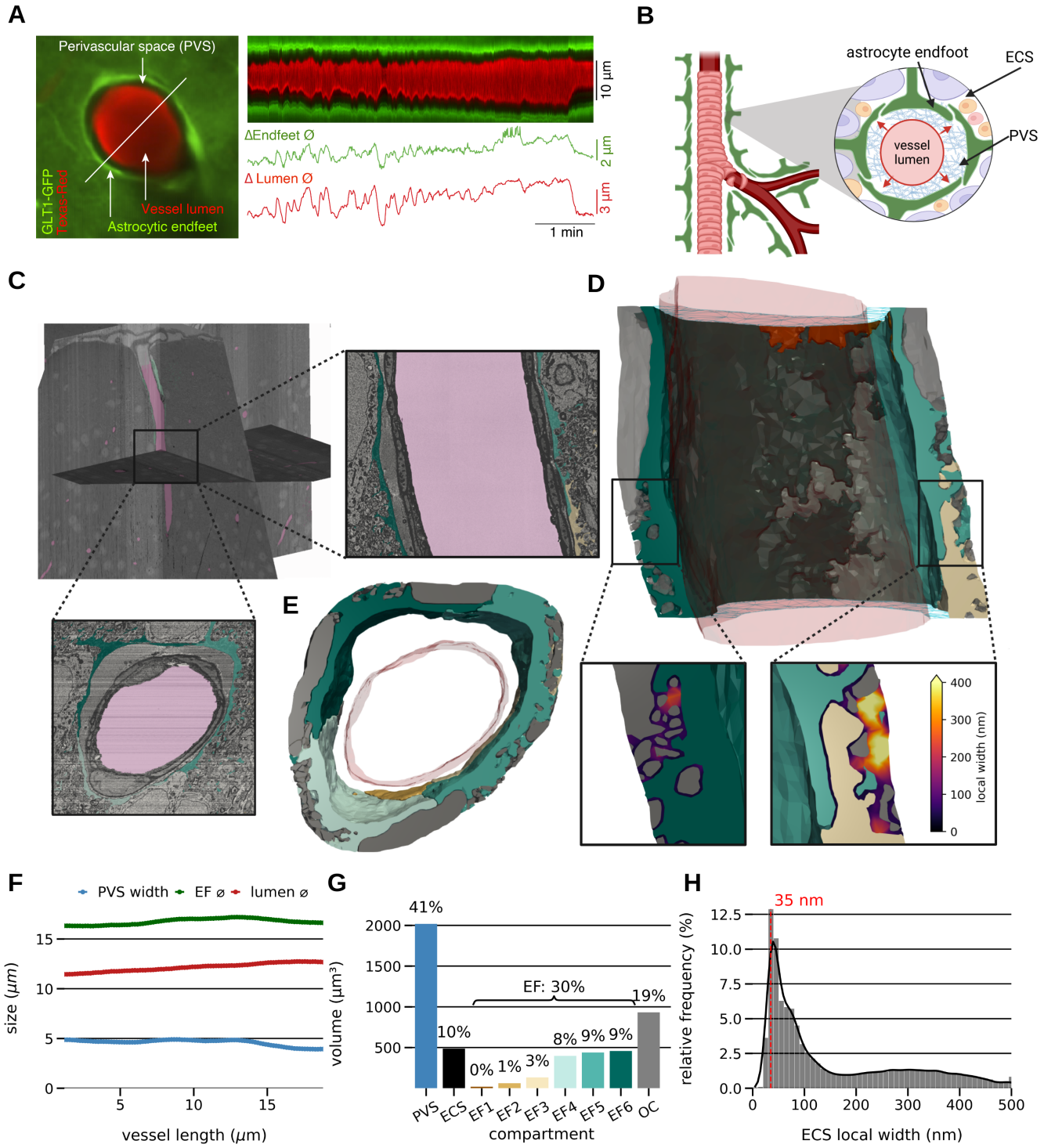

Figure 1. Geometrically-detailed reconstructions of the extravascular cellular environment enable high-fidelity simulations of the glio-vascular interplay. A) Two-photon imaging of a penetrating arteriole shows dynamic and substantial changes in endfoot sheath diameter (green) and PVS width (black) following vessel dilation and constriction (vessel lumen in red) (adapted from Bojarskaite et al. 2023, [Bojarskaite et al., 2023]) ; B) sketch of a penetrating arteriole in the mouse visual cortex and its surroundings including the PVS, ECS, and endfeet; C) electron microscopy image overlayed with the astrocyte segmentations (data extracted from the IARPA MICrONS dataset [Turner et al., 2022], interactive neuroglancer visualization). We remark that the PVS is thought to (at least) partly collapse in postmortem tissue [Mestre et al., 2020]. D) The reconstructed geometry (radial cut and zoom-ins shown), with endfeet (brown to blue-green), other cells (grey) and lumen surface (pink). The PVS and ECS are part of the geometry, but not shown here. The zoom-ins are color-coded by the local width of the extracellular space to highlight the range of gap widths (see also H); (cont. next page)

Figure 1. (**cont.**) E) Radial cut through the reconstructed geometry (colors as in D); F) average PVS width, inner endfoot sheath diameter and vessel lumen diameter along the longitudinal direction of the arteriole (values corresponding to a radially symmetric geometry of the same cross-sectional area); G) volume of the PVS, endfeet (EF1-6), other cells (OC) and ECS; H) local geometry of the non-PVS ECS, characterized by the distribution of local widths (defined per computational element as the diameter of the largest sphere fitting into the ECS and containing the element midpoint).

Stretch dominates squeeze: arteriole dilation compresses the PVS while expanding the endfoot sheath

This gliovascular environment responds to external or internal forces by distributing and balancing elastic forces and fluid motion, in a manner that depends on a number of factors (morphology, stiffness, permeability) and to an extent that is hard to predict a-priori. Therefore, to investigate the dynamics associated with typical heartbeat-derived vascular pulsations, we prescribed a 10 Hz-pulsatile dilation and contraction of the inner arteriole surface (±1%) and analyzed the resulting computational predictions of movement and force distribution within the PVS and endfoot sheath.

As expected, the dilation led the entire structure to expand (Supplementary video S1), nearly uniformly along the vessel length and synchronously, but with decreasing displacement magnitude towards the outer rim of the endfoot sheath. The mean diameter change ranged from 0.1 µm (vessel lumen) to 0.06 µm (inner endfoot sheath) at peak systole (Figure 2A). Notably, the PVS itself decreased, both in width (−0.01 µm) and volume (−0.03%) (Figure 2A–C). In contrast, the astrocyte endfoot volume remained almost constant (+0.001%), while the ECS volume increased (0.13%) (Figure 2C). The largest local increases in ECS volume occurred in the vicinity of the tight inter-endfeet gaps (up to 0.6%, Figure 2D). Thus, in terms of overall volumes, the compression of the endfoot sheath due to arteriole dilation was overcompensated by the stretch induced by its increased radius.

The mean fluid pressure in the PVS and in the ECS increased by up to 1.3 Pa and 0.3 Pa, respectively, with the PVS fluid pressure peaking in sync with the peak arteriole dilation (Figure 2E–F, Supplementary video S2). On the other hand, the pressure within the astrocytic endfeet dropped by -1.0 Pa. This, seemingly counter-intuitive, reduced pressure at peak arteriole dilation is a direct consequence of the corresponding increase in endfoot volume. In turn, these pressure differences induced fluid exchange back and forth between the PVS and the endfoot sheath over time. Interestingly, the flow rates through the endfoot gaps strongly dominated those through the adluminal endfoot membrane, peaking at 29 $\mu m^3/s$ versus at 0.01 $\mu m^3/s$, with peak flow velocities in the endfeet gaps of about 0.8 µm/s (Figure 2G–H). In addition, the fluid exchanged between the endfoot sheath and the outer surroundings. The drop in endfoot fluid pressure during arteriole dilation pulled fluid in at rates up to 1.8 $\mu m^3/s$ through the continuation of the astrocyte process. Simultaneously, we observed flow, though of lower magnitude and opposite directionality, through the extracellular space: fluid moves to and from the surrounding tissue via the outer extracellular surface at rates up to 0.23 $\mu m^3/s$ (Figure 2I). Thus, most of the fluid crossing the endfeet gap contributes to an increase of the ECS volume within the endfoot sheath and does not penetrate further into the surrounding tissue.

Examining the mechanical stresses, we found the highest mean von-Mises stress in the astrocyte endfeet (up to 4.5 Pa at peak systole) and substantially lower stress on the PVS and ECS (1.4 Pa and 1.3 Pa peak mean stress, respectively, Figure 2J).

PVS stiffening reverses gliovascular flow dynamics

PVS morphology and composition change with aging, potentially due to perturbed parenchymal macrophage activity or plaque deposition [Mestre et al., 2022, Drieu et al., 2022]. Assuming that such structural changes modify the elastic properties of the PVS, we ask how stiffness affects the mechanical interaction between the vascular pulsations, the PVS and endfoot sheath, with particular attention to the inter-endfoot flow patterns and fluid exchange (Figure 3A).

Interestingly, PVS stiffening transforms PVS volume dynamics in response to cardiac-driven vascular pulsations. While we until now had observed a decrease in PVS volume in response to the vessel dilation, the behavior was reversed by an increase in PVS stiffness: an 8× stiffer PVS yields a volume *increase* of similar magnitude as the previously observed volume *decrease* (Figure 3B). We attribute this phenomenon to a change in the relative strength of two effects. On the one hand, the PVS is radially compressed due to vessel dilation; on the other hand, the outer PVS is tangentially stretched due to an increase in PVS radius. Stiffening reduces the compression, and thus outer stretch dominates at vessel dilation. Moreover, this also implies that at a certain PVS stiffness, stretch and compression balance each other, leading to an almost constant PVS volume. Our simulation results indicate that this occurs at approximately a 4× increase in PVS stiffness compared to our baseline (Figure 3B).

These changes in volume dynamics in turn induced a reversal in pressure and flow behaviour. Comparing with the baseline PVS pressure increase of 1.3 Pa at peak dilation, we found a comparable pressure decrease with an 8× stiffer PVS, and almost constant PVS pressure over time at 4× increased PVS stiffness (Figure 3C–F). We also observed substantial changes in the endfoot gap flow. In our baseline model, fluid flows from the PVS through the endfoot gaps into the ECS at peak vessel dilation, while higher PVS stiffnesses yield flow into the PVS (Figure 3G–H). In the scenario with a 4× increase in PVS stiffness, the fluid exchange between the PVS and the parenchyma was substantially reduced. These effects on gliovascular fluid exchange

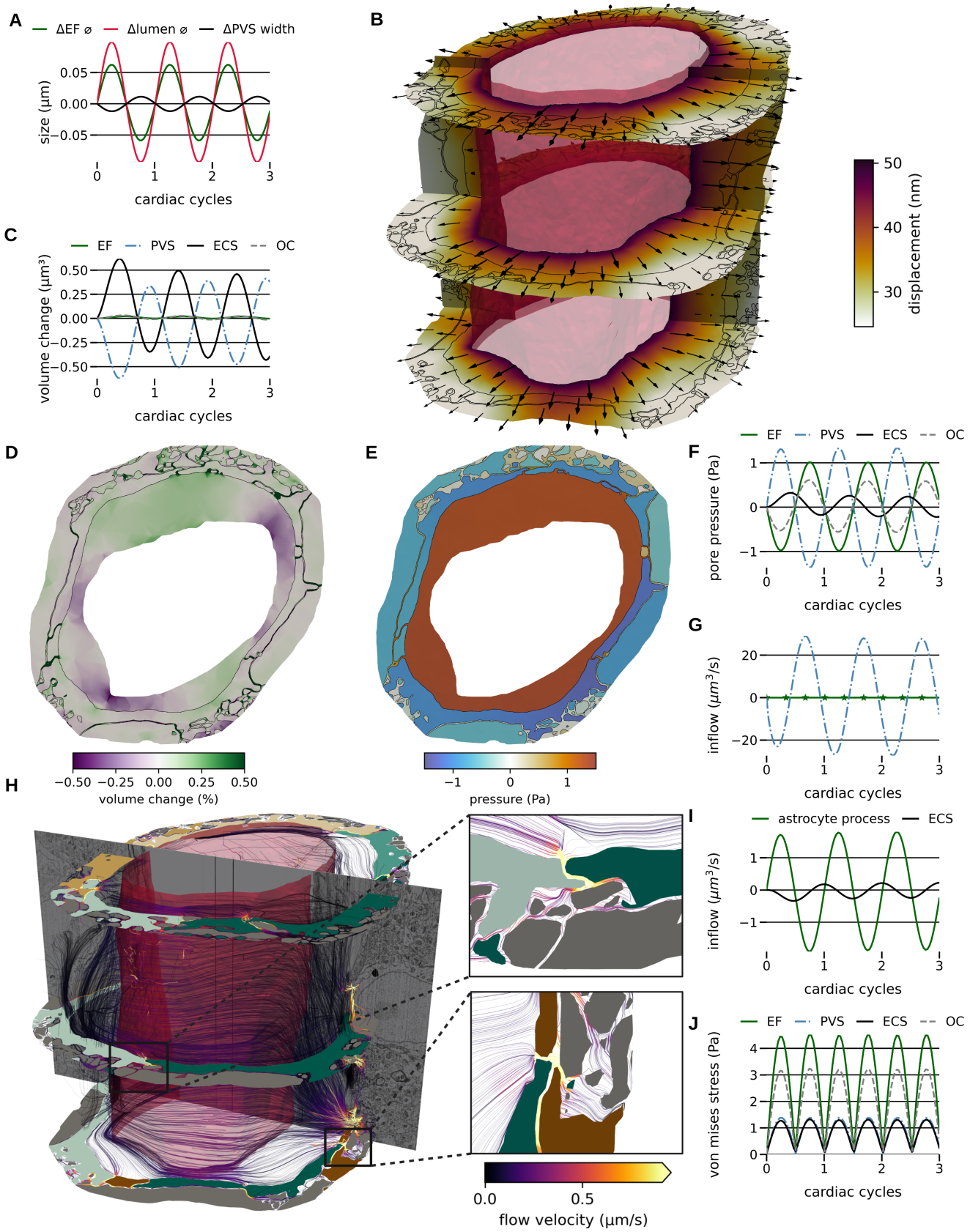

Figure 2. Stretch dominates squeeze: endfoot sheath response to cardiovascular pulsations A) Change of mean lumen diameter, endfoot sheath diameter, and PVS width over three cardiac cycles; B) displacement magnitude at peak arterial dilation: cross-sectional and longitudinal slices color-coded by displacement magnitude, arrows indicating displacement direction, cell membranes outlined in black, vessel lumen in transparent red; C) volume change of endfeet (EF), PVS, ECS and other cells (OC) over time; (cont. next page)

Figure 2. (**cont.**) D) volume change at peak arterial dilation (cross-section); E) fluid pressures at peak arterial dilation (cross-section); F) mean fluid pressures of the endfeet, PVS, ECS and other cells over time; G) flow rates *into* the PVS via the adluminal endfoot membrane (dot-dashed, blue) and through the endfoot gaps i. e. the interface between PVS and endfoot sheath ECS) (solid with stars, green) over time; H) flow streamlines in the PVS and ECS at peak systole with cross-sections through the endfeet and other cells (colors as in the Figure 1) and vessel lumen (transparent red); flow streamlines colored by the velocity magnitude; zoom-ins illustrate rapid flow through the endfeet gaps. I) Flow in through the outer radial boundaries: inflow rates for the astrocyte processes (AP, outer boundary of the astrocyte endfeet) and the ECS outer boundary; J) mean von-Mises stress of endfeet, PVS, ECS and other cells.

would likely have a profound impact on solute exchange between the PVS and surrounding tissue driven by oscillatory flow and mixing.

In addition to the effect of PVS stiffness on fluid flow rates (Figure 3G–H), we systematically investigated the effect of PVS stiffening on the pressure differences, mean fluid velocities, stress and displacement magnitudes (Figure 3I–L). Our analysis showed that the pressure difference across the adluminal endfoot membrane decreased with increasing PVS stiffness, and consequently also the resulting peak flow rates. In contrast, the peak pressure difference across the complete endfoot sheath depends nonlinearly on the PVS stiffness; dropping from 1× to 2× to 4× but then increasing from 4× to 6× to 8×, and in fact reached the same magnitude at 8× stiffer PVS (but with the opposite phase) (Figure 3I). In terms of mean fluid velocities, PVS stiffening led to a moderate increase in intracellular flow (in the endfeet and other cells), while reducing PVS flow velocities by more than a factor 2 (Figure 3J). As for the endfoot gap flow rates and endfoot sheath pressure gradients, the mean flow velocities in the ECS first dropped, but then increased and even exceeded the baseline model as the PVS stiffness increased (Figure 3J). Finally, PVS stiffening increased stress on the solid components of all compartments, most prominently in the PVS, while the peak mean displacement rose only slightly (Figure 3K–L).

Robustness and sensitivity to perivascular pathway resistance

Considering that the resistance of the perivascular pathway is subject to substantial debate [Bakker et al., 2016, Rey and Sarntinoranont, 2018, Tithof et al., 2019, Ladrón-de Guevara et al., 2022, Bohr et al., 2022, Boster et al., 2024, Gjerde et al., 2024, Quirk et al., 2024], a natural question is to what extent the previous observations depend on the flow features within the PVS. There, we considered the extreme case of a *maximal* perivascular pathway resistance, corresponding to fluid moving primarily radially within and from the PVS, by prescribing zero flow at both ends (front/rear) of the PVS. To also consider the other extreme, a perivascular pathway with *minimal* resistance, we allow the fluid to move freely in and out of the PVS at the rear end, with parameters otherwise as at baseline (Figure 4A).

The two scenarios induce clearly different PVS flow patterns: the minimal resistance scenario resulted in oscillatory axial flow with linearly increasing velocities towards the rear end reaching up to 2 µm/s, while we found a slower, more heterogeneous flow pattern converging towards the endfeet gaps in the maximal resistance scenario (Figure 4B–C). The lower resistance also resulted in lower PVS pressures (peaking at 1.0 Pa vs 1.3 Pa). Conversely, radial CSF flow rates and fluxes were reduced in the low resistance scenario, most strikingly through the endfoot gaps (-43%) (Figure 4D–E). The reduced radial flow was reflected by smaller pressure differences across the endfoot membrane (-32%) and across the whole endfoot sheath (-41%) (Figure 4F). While the mean fluid velocity in the PVS rose by more than five-fold, the flow in the ECS and within the endfeet slowed down by -30% and -10%, respectively (Figure 4G). The reduced resistance was also accompanied by smaller stresses in the endfeet and extracellular matrix, larger stress in the PVS, and smaller displacements overall (on the order of ± 10%) (Figure 4H–I). Examining the overall diameter changes of the endfoot sheath, the PVS width and the synchronicity of the system, we found a minor reduction in endfoot diameter changes and an increase of PVS width changes with lower resistance, and endfoot and vessel movement remained in synchrony.

Finally, we remark that, in contrast to the maximal resistance model, the low resistance simulation results depend on the length of the vessel segment, and with increasing segment length, the cumulative resistance increases. Thus, the maximal resistance model can be interpreted as a long-segment limit of the minimal resistance model. We conclude that the maximal resistance model is the more relevant case here, and consider the deviations in radial motion (between 7 and 58%) as upper bounds of the error of this assumption.

Astrocytic endfoot response to vascular pulsations is resilient to changes in endfoot water permeability

Astrocyte endfeet are heavily polarized with a higher density of AQP4 on the adluminal endfoot membrane compared to the abluminal side. Asking whether increased endfoot water permeability mediated by AQP4 alters the mechanical interplay between the vessel, PVS and endfoot sheath, we introduced a computational AQP4-knockout model – defined by a seven-fold reduction in the adluminal membrane permeability – and compared it with the computational wildtype model (Figure 5A). The

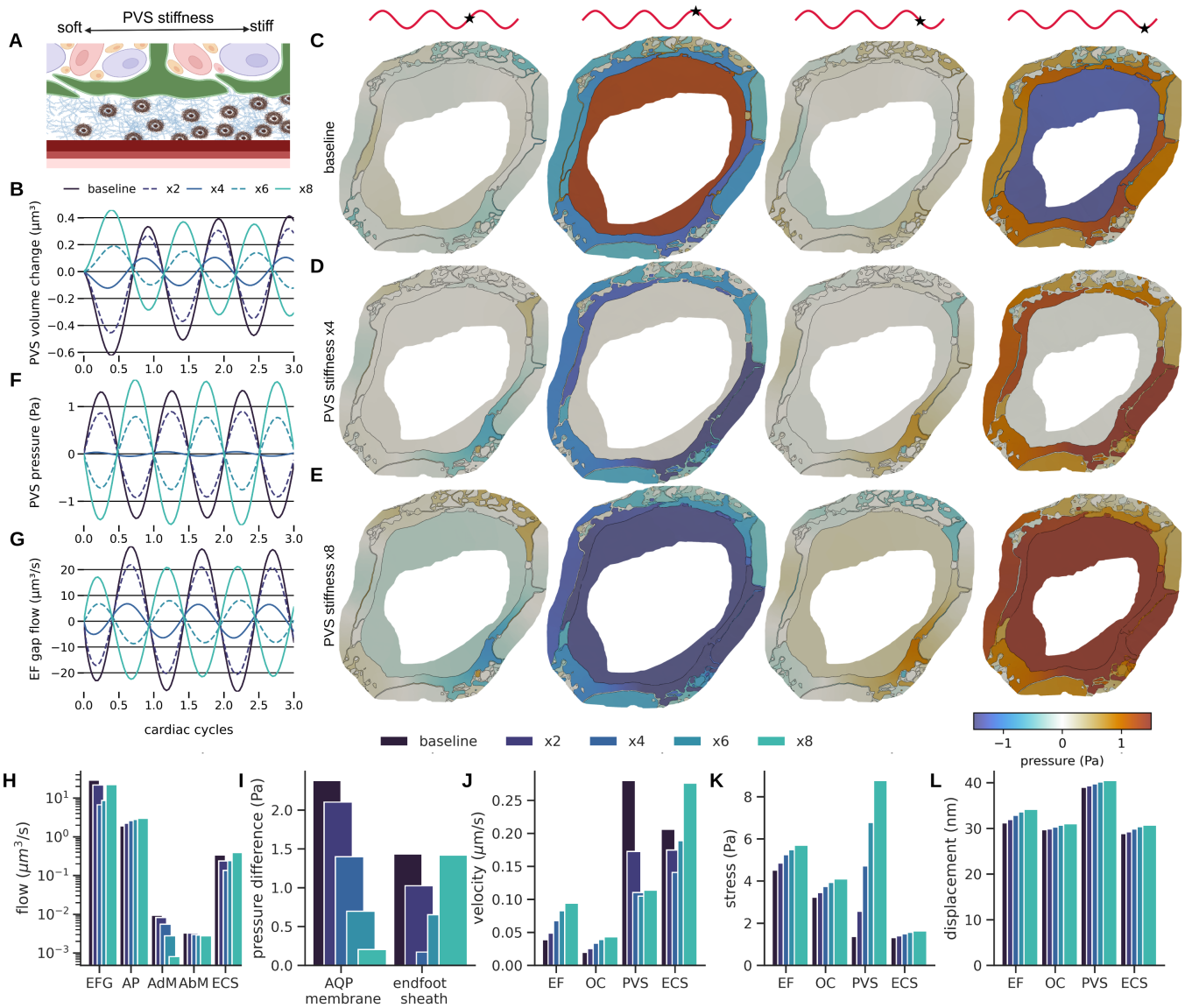

Figure 3. A) Conceptual illustration of PVS stiffening due to e.g. plaque accumulation or changes in the extracellular matrix composition; B) change in mean PVS volume over time for models with an increase in PVS stiffness by a factor of 1, 2, 4, 6, and 8. C–E) cross-section of the geometry, showing the fluid pressure over one cardiac cycle for the baseline model (C), PVS stiffness increased by 4× (D) and 8× (E); F) mean PVS pressure over time; G) flow through the endfoot gaps over time; H) peak fluid flow rates across the endfoot gaps (EFG, interface between PVS and ECS), the outer astrocyte process (AP, outer radial model boundary of the endfeet), the adluminal endfoot membrane (AdM), the abluminal endfoot membrane (AbM) and the ECS outer radial boundary (ECS); note the logarithmic scale. I) Peak mean pressure gradient across the adluminal endfoot membrane and the whole endfoot sheath; J) peak mean flow velocities in each compartment; K) peak mean von-mises stress in each compartment; L) peak mean displacement magnitude in each compartment.

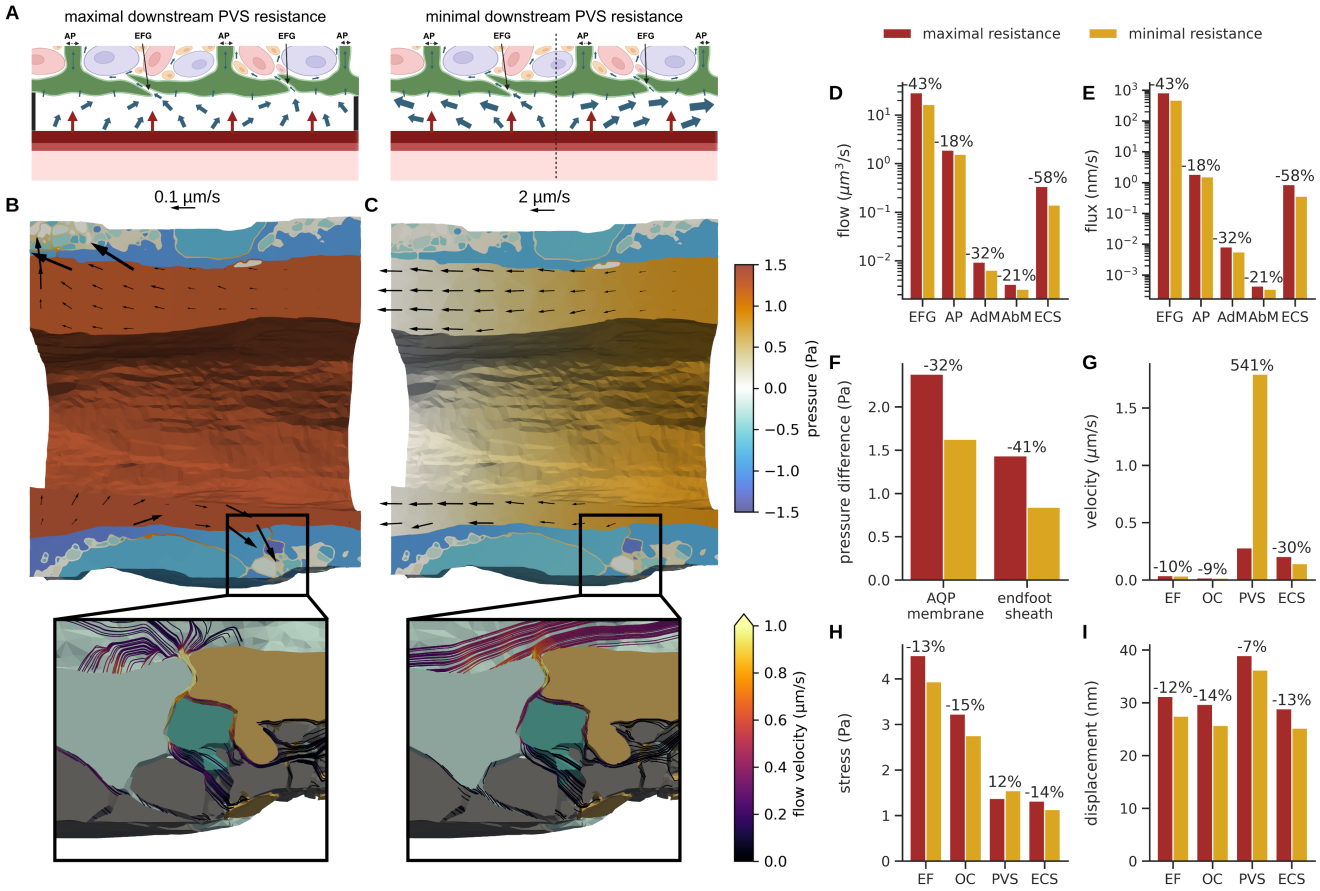

Figure 4. The downstream PVS resistance affects local flow patterns and tissue motion. A) Conceptual illustration of minimal and maximal downstream PVS resistance, B–C) fluid pressure and velocity at peak systole for the maximal downstream PVS resistance (B) and minimal PVS flow resistance scenarios (C), with zoom-ins showing streamline visualizations of extracellular fluid flow; D) peak fluid flow rates across the endfoot gaps (EFG, interface between PVS and ECS), the outer astrocyte processes (AP, outer radial boundary of the endfeet), the adluminal endfoot membrane (AdM), the abluminal endfoot membrane (AbM), and the ECS outer radial boundary (ECS); E) peak flux rates (labels as in C); F) peak mean pressure gradient across the adluminal endfoot membrane and the whole endfoot sheath; G) peak mean flow velocities in each compartment; H) peak mean von-mises stress in each compartment; I) peak mean displacement magnitude in each compartment.

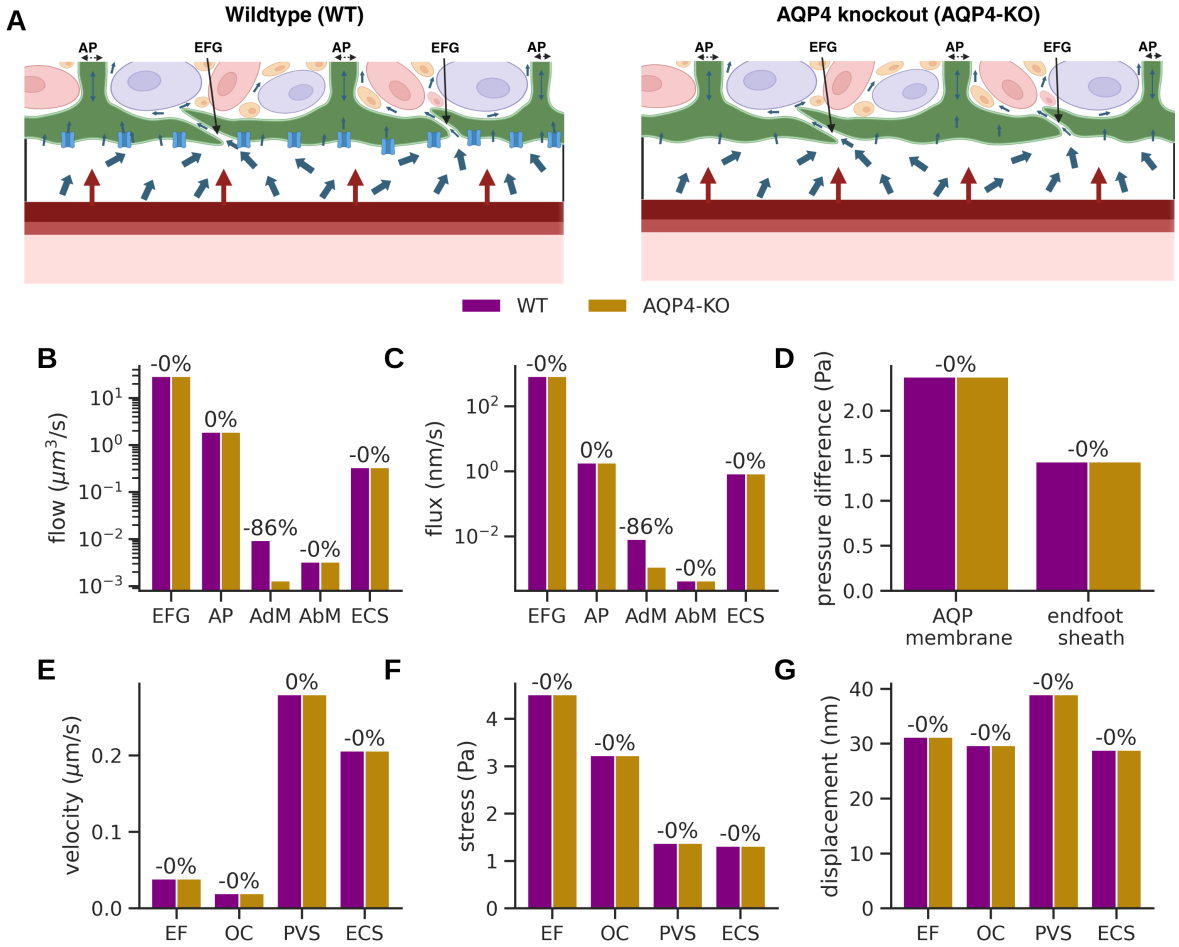

Figure 5. AQP4-mediated increase in water channels have a negligible impact on gliovascular dynamics. A) Conceptual illustration of the computational wildtype and AQP4 knockout models; B) peak fluid flow rates across the endfoot gaps (EFG, interface between PVS and ECS), the outer astrocyte process (AP, outer radial boundary of the endfeet), the adluminal endfoot membrane (AdM), the abluminal endfoot membrane (AbM) and the ECS outer radial boundary (ECS); C) peak flux rates (labels as in C); D) peak mean pressure gradient across the adluminal endfoot membrane and the whole endfoot sheath; E) peak mean flow velocities in each compartment; F) peak mean von-mises stress in each compartment; G) peak mean displacement magnitude in each compartment;

seven-fold difference in permeability is based on experimental data acquired at room temperature, and may be an overestimation of the effect at physiological temperatures [Solenov et al., 2004]. As expected, we found a considerable relative decrease in fluid flow across the endfoot membrane with each vessel pulsation (-86%, Figure 5B–C). However, due to the small magnitude of the transmembrane flux in both scenarios (smaller than 0.1 nm/s), neither pressure differences, endfoot stresses or displacements, nor other flow velocities, showed substantial differences (all fell below a 1% relative difference) (Figure 5B–G). Thus, the overall dynamics of the PVS and endfoot sheath driven by vascular pulsations were virtually indistinguishable for the wildtype and the reduced adluminal permeability models.

Osmotic challenge drives AQP4-enhanced net fluid flow

Blood osmolytes such as glucose have been suggested as potential drivers of brain fluid flow [Bork et al., 2024], with reported persistent concentration differences between vascular and extracellular glucose amounting to 4 mM [Patching, 2017]. Noting that the constant supply of glucose requires a spatial concentration gradient across the gliovascular interface, we hypothesized that perivascular glucose might be elevated compared to the surrounding tissue, and more specifically, glucose levels might be elevated compared to the astrocyte endfeet. Here, we investigated whether and to what extent adding osmolytes in the gaps between the endfoot and vessel could drive fluid flow in the model, and how the presence of AQP4 water channels affects gliovascular mechanics under such conditions. Concretely, we considered a scenario without vascular pulsations but prescribed

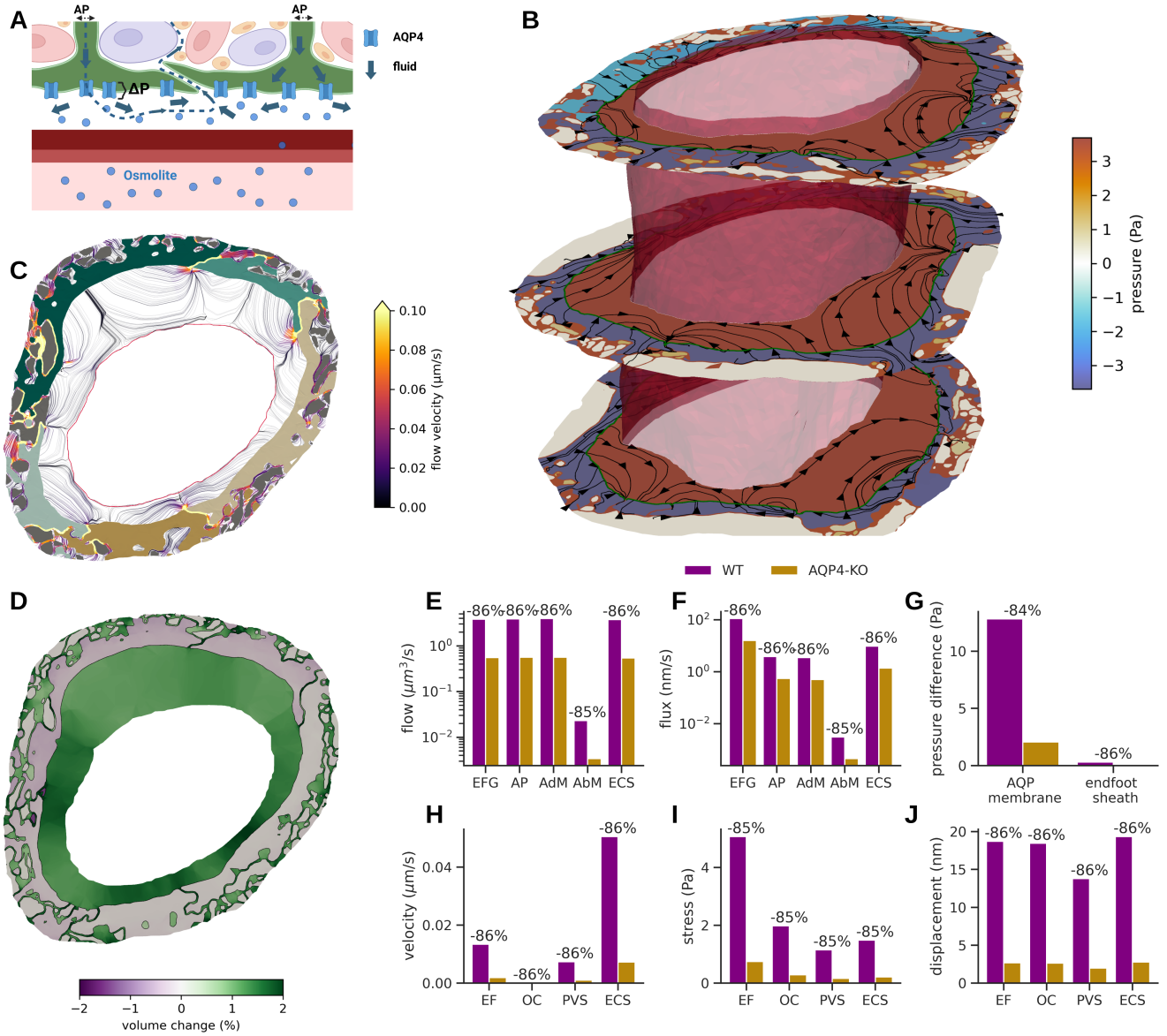

Figure 6. Osmotic differences can drive fluid exchange between the PVS and its surrounding tissue that depends on AQP4 density. A) A blood osmolyte such as glucose permeates the PVS, potentially inducing an osmotic pressure difference across the endfoot membrane facing the vessel, yielding a persistent flow through the endfoot, into the PVS and further through the endfoot gaps into the surrounding tissue. B) The fluid pressure and flow streamlines in the endfeet, ECS and PVS (cross-section) induced by the osmotic pressure difference; C) extracellular fluid flow velocities (streamlines colored by velocity magnitude); D) relative volume change; E) mean fluid flow rates across the endfoot gaps (EFG, interface between PVS and ECS), the outer astrocyte process (AP, outer radial boundary of the endfeet), the adluminal endfoot membrane (AdM), the abluminal endfoot membrane (AbM) and the ECS outer radial boundary (ECS); F) mean flux rates (labels as in E); note the logarithmic scale in E) and F). G) Mean pressure gradient across the adluminal endfoot (AQP) membrane and the whole endfoot sheath; H) flow velocities in each compartment; I) mean von-mises stress in each compartment; J) mean displacement magnitude in each compartment.

an osmotic pressure gradient of 1 kPa - corresponding to an osmolyte concentration difference of 0.39 mM - across the endfoot membrane facing the blood vessel as an alternative driving force (Figure 6A).

The osmotic pressure gradient induced a steady, swirling flow pattern, with a flow rate of 3.8 $\mu m^3/s$ across the endfoot membrane leading to a pressure increase of about 4 Pa in the PVS (Figure 6B). The intracellular fluid pressure dropped by up to 5 Pa, with considerable variations between the endfeet depending on their surface area exposed to the osmotic gradient. The resulting pressure gradients induced both intra- and extracellular net fluid flow: the intracellular pressure drop pulled fluid from the surrounding tissue via the intracellular pathway into the endfoot, while the increased PVS fluid pressure drove ISF through the endfoot gaps into the extracellular space and further into the surrounding tissue, creating a persistent mechanism for fluid exchange between the PVS and the surrounding cerebral tissue (see conceptual illustration in Figure 6A). Peak endfoot gap flow velocities reached up to 100 nm/s in this scenario (Figure 6C). Additionally, the elevated PVS pressure also induced an increase in PVS volume by up to 2%, while endfoot volumes decreased slightly (Figure 6D).

Finally, we asked how the water permeability of the astrocytic endfoot membrane would affect this osmotically-induced fluid flow. Again inspired by the reduced water permeability measured in AQP4 knock-out mice [Solenov et al., 2004], we decreased the adluminal membrane permeability by 7× before repeating the simulation. In this scenario, the seven-fold reduction in membrane permeability directly translated into a seven-fold reduction in transmembrane fluid flow (-86%), and subsequently the same relative reduction in flow through the astrocyte processes, endfeet gaps, and ECS (Figure 6E–F). Indeed, we observed an equal relative reduction in all other quantities of interest, including the pressure difference across the adluminal membrane and endfoot sheath, mean fluid velocities, stress and mean displacement in each compartment (Figure 6G–J). Although this modelling scenario is based on assumptions that are not possible to experimentally verify with current technology, it illustrates how osmotic driving forces at the gliovascular interface may be a potent driver of directional fluid flow on the microscale, and that AQP4 may play a key role in this mechanism.

Discussion

We have presented a detailed computational model of the interplay between solid and fluid mechanics of astrocyte endfeet at the gliovascular interface with realistic high-resolution geometries derived from electron microscopy. A key model prediction is that during arteriole dilation, the PVS is compressed while the endfoot sheath expands, leading to increased fluid pressure in the PVS and decreased pressure within the endfeet. Fluid flow then occurs predominantly through the inter-endfeet gaps rather than through the AQP4-rich astrocyte membrane. An interesting observation that may be important for understanding extracellular fluid dynamics in aging and pathology is that increasing the stiffness of the PVS reversed the PVS volume, pressure and flow dynamics across the cardiac cycle – in some cases, resulting in minimal fluid exchange between the PVS and surrounding tissue. Hence, the PVS composition of extracellular matrix and cells may strongly affect gliovascular dynamics and endfoot–parenchymal fluid exchange. The resistance of the downstream perivascular pathway affects local flow patterns, with lower resistance leading to reduced radial flow and increased axial flow within the PVS, but only minor changes in endfoot stress and displacement. A substantial reduction in AQP4-mediated water permeability negligibly impacts the gliovascular dynamics associated with heart-beat-induced vascular pulsations, including flow velocities, pressure differences, stress, and displacements, despite a considerable relative increase in fluid flow across the endfoot membrane. Instead, the AQP4-rich adluminal astrocyte endfoot membrane will enhance fluid exchange between the PVS and surrounding tissue if driven by a osmotic pressure gradient.

While both oscillatory and directional net flow of CSF along the PVS have been extensively studied in both animal [Drieu et al., 2022, Mestre et al., 2018, Holstein-Rønsbo et al., 2023] and mathematical models [Bakker et al., 2016, Rey and Sarntinoranont, 2018, Tithof et al., 2019, Ladrón-de Guevara et al., 2022, Boster et al., 2024, Gjerde et al., 2024, Quirk et al., 2024], the dynamic mechanical interplay between the blood vessel, the PVS and the endfeet is less studied. Recent data clearly demonstrate that astrocyte endfeet move with blood vessel dynamics, especially during sleep [Bojarskaite et al., 2023], but the outer boundary of the PVS and the endfeet themselves are typically modelled as a rigid sheath. A notable exception is the study by Kedarasetti et al. [2022], in which the authors also modelled a poroelastic (but homogenized) tissue surrounding the PVS. To the best of our knowledge, ours is the first computational model of the gliovascular interface using detailed, realistic geometries that capture the complex morphology of the astrocyte endfoot sheath, and thus enable high-fidelity simulations of flow through the endfoot membrane and the inter-endfoot gaps. Our poroelastic modelling approach describes the complex interaction of mechanical forces, deformation and fluid flow - both within extra- and intracellular spaces and across cell membranes - and thus constitutes a foundational model for computational studies of mechanical forces in the nervous system. In the light of the emerging role of mechanobiology in neuroscience [Pillai and Franze, 2024, Tyler, 2012, Procès et al., 2022], our model establishes a starting point for future in-silico studies of cellular mechanics, especially in combination with dense neuronal tissue reconstructions.

Turning to model validation, we first note that due to the immense difficulty of measuring many of the relevant quantities in vivo, several of our computational predictions lack experimental counterparts. However, both Holstein-Rønsbo et al. [2023] and

Bojarskaite et al. [2023] report that arterial dilation by whisker-stimulation-induced hyperemia and sleep state changes directly affect the PVS width in head-fixed mice. They describe that arterial dilation induces an dilation of the endfoot sheath, but with a lower magnitude, thus reducing the width of the ensheathed PVS. This aligns well with our findings. Holstein-Rønsbo et al. [2023] also report a radial displacement of the surrounding tissue of 0.8 µm in response to whisker stimulation - supporting our modelling assumption that vessel dilation also triggers displacement beyond the immediate endfoot sheath. Moreover, Holstein-Rønsbo et al. [2023] report an increase of both radial and axial PVS flow velocity after whisker stimulation, with radial velocities in the order of 0-4 µm/s. We found substantially lower peak mean radial PVS flow velocities (0.28 µm/s), consistent with a much smaller arterial diameter change (6% vs 1%). In terms of intracellular cytosol flow rates, our estimates (up to 0.03 µm/s peak mean velocity in the endfeet) align well with typical values for cytosolic flow rates of approximately 0.01–1 µm/s [Mogilner and Manhart, 2018]. We are not aware of any reports on the mechanical stress in astrocyte endfeet during physiological pulsations, but our computational predictions of up to 5 Pa fall at the lower end of typical stresses in the cytoskeletal mesh of up to hundreds of pascals [Mogilner and Manhart, 2018]. In addition, we observed pressure gradients in the order of 1 Pa/µm, again lower than characteristic values of 10 Pa/µm. However, considering that cardiac-induced motion is a low displacement and stress regime compared with e.g. hyperemia or pathological conditions such as ischemia or cortical spreading depression, supports these comparably low pressure and stress predictions. Furthermore, assessing our transmembrane flux rates ranging around 10^{-2} nm/s in the cardiac-induced scenario and around 10 nm/s in the osmotically-driven scenario, we find good agreement with characteristic flow rates across membranes of 1–10 nm/s at characteristic pressures of 100 Pa [Mogilner and Manhart, 2018], if the difference in transmembrane pressure gradients is taken into account.

The composition and morphology of the PVS changes with aging and in disease, potentially due to accumulation of extracellular matrix proteins or plaque deposition [Mestre et al., 2022, Drieu et al., 2022]. Investigating how changes in PVS elastic properties affect gliovascular mechanics, we found that PVS stiffening reverses the flow dynamics between the PVS and its surrounding tissue: a soft PVS compresses with vessel dilation and pushes fluid through the endfoot gaps, while a substantially stiffer PVS experiences a larger tangential stretch than radial compression and draws fluid through the endfoot gap. While these two cases lead to oscillatory fluid exchange with similar magnitude and opposing phase between PVS and surrounding tissue, an interesting third case emerges: at a certain PVS stiffness, radial compression and tangential stretch of the PVS balance each other, resulting in (almost) no fluid exchange across the endfoot sheath. This scenario arose at about a four-fold increase in PVS stiffness compared to our baseline model, providing a mechanistic explanation for reduced glymphatic flow with PVS plaque accumulation and perivascular stiffening.

An interesting question is whether the endfeet could potentially act as one-way valves for interstitial fluid flow by changing their gap size in response to pressure changes, as recently proposed by Bork et al. [2023] and Gan et al. [2023]. Our results show that the extracellular space volume between the endfeet indeed increases in response to cardiac-induced arterial dilation, albeit only by approximately 0.1%. Whether this would translate to a sufficient reduction in flow resistance and enable a valve-like effect of the endfoot sheath stands as unclear.

In our modelling, we focused on the radial interplay of the vessel, PVS and endfoot, and did not seek to explain directional PVS flow, as it likely emerges on the larger spatial scale of a vessel network, rather than a single short vessel segment [Gjerde et al., 2024] and/or due to asymmetry. Still, we can not completely ignore the role of axial PVS flow, as it also impacts radial mechanics. Given the substantial uncertainty about PVS properties in general and resistance in particular, we studied and compared the extremes and found that even the minimal downstream PVS resistance reduced radial flow and tissue forces by only 7–58% compared with a maximal resistance scenario. Interpreting the maximal resistance scenario as the model's long-segment limit, we consider these ranges as upper error limits of the simplifying assumption of our choice of the maximal resistance model.

The physiological role of AQP4 water channels has been the subject of considerable research activities over the last decade [Mathiisen et al., 2010, Nagelhus and Ottersen, 2013], and AQP4 has been suggested to support glymphatic clearance by facilitating water exchange across the endfoot sheath [Mestre et al., 2020]. However, our results show that AQP4 has almost no impact on the mechanical interaction between vessel and endfeet, primarily because the resistance of the endfoot gap is orders of magnitude smaller than both an AQP4-rich and AQP4-void membrane. This finding aligns with previous estimates of the endfoot sheath permeability [Koch et al., 2023, Jin et al., 2016, Hladky and Barrand, 2022] but does not provide a satisfactory answer to the question of the physiological role of AQP4, especially given the notable abundance of AQP4 channels, and the impact of AQP4 knockout in animal models [Mestre et al., 2020].

Drawing from earlier experimental findings demonstrating the importance of AQP4 in influencing osmotically driven water influx, specifically in brain edema [Manley et al., 2000, Amiry-Moghaddam et al., 2003, Papadopoulos et al., 2004], we asked under which physiological conditions AQP4-mediated water flux could play a more decisive role. Concretely, we hypothesized that perivascular glucose might be elevated compared to the adjacent tissue (and specifically the endfoot) and imposed an osmotic pressure gradient across the adluminal endfoot membrane. In such a scenario, the difference in osmolarity creates a circular flow pattern: intracellular pressure differences drive fluid from the astrocyte cell body to the endfoot membrane, where

it crosses into the PVS, leading to an increase in PVS volume and pressure, which consequently drives fluid through the endfoot gaps into the surrounding ECS. Interestingly, we observed that this mechanism is highly sensitive to the endfoot membrane permeability: a sevenfold reduction in permeability - mimicking the absence of AQP4 channels - reduced flow sevenfold, suggesting that AQP4 water channels' primary role is in facilitating osmotically, not hydrostatically driven fluid exchange. While the idea that blood osmolytes might drive fluid flow across the gliovascular interface has been suggested previously [Bork et al., 2024, Jin et al., 2016], the existence of such a gradient is far from certain. However, well-established differences between blood and brain extracellular space glucose levels [Patching, 2017], and the necessity of a constant supply of glucose across the blood-brain-barrier, suggest a glucose concentration gradient across the gliovascular interface and potentially also at the adluminal endfoot membrane. In addition, we remark that our modelling is independent of the specific cause of osmotic imbalance, and remains relevant for other scenarios involving osmotic pressure differences at the gliovascular interface. Due to the linearity of the model, flow rates scale linearly with the imposed osmotic gradient.

The high spatial resolution of electron microscopy allowed us to create a highly detailed reconstruction of the astrocyte endfeet, but also comes with limitations, primarily the shrinkage of extracellular space due to chemical fixation. In particular, the inter-endfeet gap width is crucial for the endfoot sheath permeability, yet has not been accurately measured in living tissue. After processing the cell segmentation with our processing pipeline (see Methods), the distribution of extracellular space local width peaked at about 35 nm corresponding to the endfoot gap size, which is only slightly larger than the value of 20 nm reported by Mathiisen et al. [2010] (also based on EM imaging). While a potential overestimation of endfoot gap size favors flow through endfoot gaps over transmembrane flow, we note that it does not fundamentally change the flow ratio of more than three orders of magnitude. Similarly, the local width of ECS beyond the endfeet gaps in our geometry is heavily influenced by our image-processing pipeline. However, the advent of new imaging technologies such as super-resolution shadow imaging (SUSHI) [Tønnesen et al., 2018] has enabled accurate characterization of the local geometry of the extracellular space. Here, we found that the local extracellular space width in our reconstructed geometry aligns well with the observations of a highly heterogeneous ECS, ranging from small gaps between 10–20 nm to larger pools of 200–500 nm [Tønnesen et al., 2023]. In terms of the PVS geometry, we chose to identify the entire space between the vessel lumen and the astrocyte endfeet as PVS, which reflects the viewpoint of two-photon imaging and resulted in a PVS width of approximately 5 µm, which is in good agreement with previously reported values [Bojarskaite et al., 2023].

In terms of limitations beyond the uncertainty about geometrical features of the PVS and endfoot sheath, one of our primary modelling constraints is the assumption of linear poroelastic media for the intra- and extracellular space. While being a good first-order approximation, it is well known that biological tissue is often characterized by nonlinear stress-strain relations with memory and elements of plasticity [Mogilner and Manhart, 2018]. For instance, the collagen networks that are a major component of the extracellular matrix can be substantially stiffer under tension than compression, and rather buckle than compress under compressive loading [Kedarasetti et al., 2020]. However, accounting for the inherent nonlinear mechanics increases the computational cost considerably, and requires detailed knowledge of the material behaviour to parameterize and advantageously employ such a model. Furthermore, our analysis is based on an idealized waveform of arterial pulsations due to a lack of data at sufficient temporal resolution. While imperfect, we rate this to be a sufficiently accurate representation of the actual arterial pulsations.

In conclusion, our model is the first to combine a comprehensive mathematical model of the poroelastic behaviour of intra- and extracellular space with a realistic, EM-derived geometry of the gliovascular interface. Our model provides detailed insights into the mechanics of blood vessels, astrocyte endfeet and their ensheathed PVS, and enables accurate predictions of their interplay. These findings supplement and extend insights from experimental studies on the role of astrocyte endfeet in health and disease, and provide a foundation for further computational studies of cellular mechanical interaction in the nervous system.

Methods

Image processing and computational geometry pipeline

Using imaging data from the EARP MICrONS dataset [Turner et al., 2022], we extracted a segmentation of the extravascular surroundings of a cortical arteriole, including several astrocyte endfeet, a perivascular space surrounding the lumen and endothelial cells, and other extracellular spaces (Figure 1C). We then generated a computational mesh of the geometry, conforming to the interior interfaces, via a custom image processing and meshing pipeline based on the fTetWild meshing software [Hu et al., 2020]. In particular, as part of the preprocessing, we inflated the computational geometry representation of the extracellular space of the endfoot sheath to 16.6% to counteract the effect of chemical fixation. The computational mesh includes 258 776 vertices and 1 425 200 cells with a mesh resolution of 0.36 ± 0.22 µm.

Poroelasticity model including material parameters

We characterize both the intracellular (astrocyte endfeet, neurons and other cells) and extracellular spaces as poroelastic structures composed of an elastic solid matrix filled with interstitial fluid (ISF) and cytosol, respectively [Mogilner and Manhart,

Parameter	Value	Ref.
Stiffness (Young modulus) E	-	
– endfeet E_{EF}	1500 Pa	Lu et al. [2006] Esteki et al. [2021]
– ECS E_{ECS}	150 Pa	
– PVS E_{PVS}	150 Pa	
Poisson's ratio ν	0.3	Lu et al. [2006] Esteki et al. [2021]
Fluid viscosity μ_F	$0.0007\,\mathrm{Pa}\cdot\mathrm{s}$	Bloomfield et al. [1998]
Biot–Willis coefficient α	1	
Storage coefficient s	$0\,\mathrm{Pa}^{-1}$	
Permeability κ	-	
– endfeet	$1\cdot 10^{-15}\,\mathrm{m}^2$	
– ECS	$2\cdot 10^{-15}\,\mathrm{m}^2$	
– PVS	$2\cdot 10^{-14}\,\mathrm{m}^2$	Kedarasetti et al. [2022], Wang and Olbricht [2011]
Membrane conductance L_p (AQP)	$3.49\cdot 10^{-12}\,\mathrm{m\,s^{-1}\,Pa^{-1}}$	Solenov et al. [2004]
Membrane conductance L_p (non-AQP)	$4.88\cdot 10^{-13}\,\mathrm{m\,s^{-1}\,Pa^{-1}}$	Solenov et al. [2004]
Far-field pressure p_{far}	0 Pa	
Far-field distance l_{far}	50 µm	
Outer stiffness E_{far}	1500 Pa	Budday et al. [2020]
Outer permeability κ_{far}	$10^{-16}\,\mathrm{m}^2$	Holter et al. [2017]
Stiffer PVS scenario	$E_{\mathrm{PVS}}\times 2,4,6,8$	

Table 1. Material parameters for the in-silico model scenarios. The Lamé parameters μ_S and λ are related to the Young modulus E and Poisson's ratio ν by $\lambda = \frac{E\nu}{(1+\nu)(1-2\nu)}$ and $\mu_S = \frac{E}{2(1+\nu)}$.

2018, Moeendarbary et al., 2013, Esteki et al., 2021], though with differing material parameters. In the intracellular space Ω_i, this elastic matrix represents the cytoskeleton, while the extracellular matrix, macromolecules, and unresolved cellular structures provide an elastic scaffold in the PVS and extracellular space Ω_e. The semi-permeable cell membrane Γ separates the intracellular and extracellular domains, while allowing for pressure-driven fluid exchange. Within this context and under the assumption of relatively small deformations [Biot, 1941], Biot's equations of linear poroelasticity predict the evolution in time and distribution in space of the pressure $p = p(\boldsymbol{x},t)$ and displacement vector $\mathbf{d} = \mathbf{d}(\boldsymbol{x},t)$, for $\boldsymbol{x} \in \Omega_i, \Omega_e$ and $t > 0$, and read as:

$$-\mathbf{div}\,(2\mu_S\boldsymbol{\varepsilon}(\mathbf{d}) + \lambda\,\mathbf{div}\,\mathbf{d}\mathbf{I} - \alpha p\mathbf{I}) = 0 \quad \text{in } \Omega_i, \Omega_e, \tag{1a}$$

$$s\partial_t p - \alpha\partial_t\,\mathbf{div}\,\mathbf{d} + \mathrm{div}\left(\frac{\kappa}{\mu_F}\nabla p\right) = 0 \quad \text{in } \Omega_i, \Omega_e, \tag{1b}$$

where $\mathbf{div}$ and div denotes the divergence acting on tensors and vectors, respectively, $\boldsymbol{\varepsilon}(\mathbf{d})$ is the symmetric strain tensor, $\mathbf{I}$ is the identity tensor, and ∂_t is the time derivative.

At the cell membrane Γ, a Robin-type interface condition allows for the transmembrane fluid flux $\mathbf{q} = -\frac{\kappa}{\mu_F}\nabla p$ to be regulated by the membrane permeability L_p, the hydrostatic pressure difference $[\![p]\!]$ and the osmotic pressure p_{osm}:

$$\mathbf{q}\cdot\mathbf{n} = L_p\left([\![p]\!] + p_{\mathrm{osm}}\right) \equiv L_p\left(p|_{\Omega_i} - p|_{\Omega_e} + p_{\mathrm{osm}}\right) \qquad \text{on } \Gamma. \tag{2}$$

For the scenario with an osmotic driving force, we link the osmotic pressure with the concentration difference Δc by the van't Hoff equation $p_{\mathrm{osm}} = \Delta c i R T$, where i is the van't Hoff index ($i = 1$ for glucose), R is the ideal gas constant and T denotes the absolute temperature. For all other scenarios we set $p_{\mathrm{osm}} = 0$. Further, imposing mass conservation, continuity of the displacement and momentum conservation on the cell membrane yields the additional constraints

$$[\![\mathbf{q}\cdot\mathbf{n}]\!] = 0, \quad [\![\mathbf{d}]\!] = 0, \quad [\![(2\mu_S\boldsymbol{\varepsilon}(\mathbf{d}) + \lambda\,\mathbf{div}\,\mathbf{d}\mathbf{I} - \alpha p\mathbf{I})\cdot\mathbf{n}]\!] = 0 \qquad \text{on } \Gamma. \tag{3}$$

These equations are parameterized by the Lamé constants $\mu_S > 0$ and $\lambda > 0$, the Biot-Willis coefficient $\alpha \in (0,1]$, the storage coefficient $s \geq 0$, the permeability $\kappa > 0$, the fluid viscosity $\mu_F \geq 0$ and the hydraulic conductivity of the cell membrane L_p (see also Table 1). We assume that the system starts at rest and at zero pressure.

Interaction with the surroundings: dynamic boundary conditions

To model the response of the tissue to vascular pulsations, we prescribe a given radial motion of the arteriole wall. Specifically, we assume that the arteriole dilates and constricts rhythmically in time with frequency f and amplitude A in the radial direction

Boundary	Label	continuity condition	momentum condition
Interface between lumen and PVS	Γ_{VW}	no flow	prescribed displacement
Axial end of the PVS (front)	$\Gamma_{\text{PVS-A}}$	no flow	no axial displacement
Axial end of the PVS (rear)	$\Gamma_{\text{PVS-B}}$	no flow | zero pressure	no axial displacement
Outer radial boundary (ICS)	$\Gamma_{\text{EF-radial}}$	far field pressure	linear resistance
Outer radial boundary (ECS)	$\Gamma_{\text{ECS-radial}}$	far field pressure	linear resistance
Axial end of the ECS (front, rear)	$\Gamma_{\text{ECS-axial}}$	no flow	no axial displacement
Axial end of the ICS (front, rear)	$\Gamma_{\text{EF-axial}}$	no flow	no axial displacement

Table 2. Summary of model boundaries, boundary conditions and boundary assumptions, using the terminology: no flow: $\mathbf{q}\cdot\mathbf{n}=0$, zero pressure: $p=0$, far-field pressure cf. (5), prescribed displacement cf. (4), no axial displacement cf. (7), linear resistance cf. (6).

$\mathbf{r}$ on Γ_{VW}, uniformly along the axial direction:

$$\mathbf{d}|_{\Gamma_{VW}}(t) = A\sin(2\pi f t)\mathbf{r}. \tag{4}$$

We thus neglect any phase shift along the vessel wall, which is a reasonable assumption here considering the high wave speed of the arterial pulse wave relative to the microscopic length of the vessel segment. Moreover, we assume that this interface is impermeable; i.e. we do not allow for fluid flow from the perivascular space into the lumen or vice versa.

At the outer radial boundary of the geometry ($\Gamma_{\text{radial}} \equiv \Gamma_{\text{EF-radial}} \cup \Gamma_{\text{ECS-radial}}$) we consider a homogenized representation of the neuropil as a soft and permeable tissue with permeability κ_{far} and stiffness E_{far}. We allow for fluid flow across both the outer extracellular and intracellular boundaries. Concretely, we assume a linear pressure profile between the outer boundary and a far-field pressure p_{far} at a distance l_{far} yielding the condition:

$$\mathbf{q}\cdot\mathbf{n} = \frac{\kappa_{\text{far}}}{\mu_F l_{\text{far}}}(p - p_{\text{far}}) \qquad \text{on } \Gamma_{\text{radial}}. \tag{5}$$

Similarly, we use an elastic spring model for the outer radial displacement: the outer endfoot sheath is allowed to dilate and constrict, but an opposing force linear to the displacement magnitude mimics the resistance of the surrounding tissue.

$$\boldsymbol{\sigma}\cdot\mathbf{n} = \frac{E_{\text{far}}}{l_{\text{far}}}\mathbf{d} \qquad \text{on } \Gamma_{\text{radial}} \quad \text{where } \boldsymbol{\sigma} \equiv 2\mu_S\boldsymbol{\varepsilon}(\mathbf{d}) + \lambda\,\mathbf{div}\,\mathbf{d}\mathbf{I} - \alpha p\mathbf{I}. \tag{6}$$

We fix the axial boundaries of the intracellular and non-perivascular extracellular spaces by not allowing for any displacement in the axial direction or any fluid flow there. More precisely, we set

$$\mathbf{d}\cdot\mathbf{e}_y = 0, \qquad [\boldsymbol{\sigma}\cdot\mathbf{n}]\cdot\mathbf{e}_m = 0 \quad \text{for } m \in \{x, z\}, \tag{7}$$

with the standard basis vectors $\mathbf{e}_x$, $\mathbf{e}_y$ and $\mathbf{e}_z$, and noting that the vessel centerline is oriented in the y-direction. However, for the axial perivascular boundary, we consider two scenarios. One side remains closed, but we set the other side to be either open (by prescribing a zero pressure) or closed (by prescribing zero flow). These two scenarios model the two extreme cases of either an infinitely small or an infinitely large resistance of the PVS fluid pathway.

For a summary of all boundary conditions, see Table 2.

Numerical approximation and simulation software

To solve the Biot equations (1) numerically, we employ a three-field formulation with the fluid flux $\mathbf{q} = -\frac{\kappa}{\mu_F}\nabla p$ as additional unknown [Hong and Kraus, 2017, Hu et al., 2017]. Discretizing in time with a finite-difference approach, we use a non-conforming discontinuous Galerkin discretization in space, which ensures local (fluid) mass conservation. This numerical approximation property is especially relevant here, as the fluid mass and the associated changes in pressure and volume are primary quantities of interest. Moreover, the scheme provides optimal (first-order) convergence rates at a low number of degrees of freedom per element [Hu et al., 2017], and is thus well-suited for high-resolution meshes of complex geometries. The total number of degrees of freedom is 12 954 440 at each time step. A comprehensive description of the numerical method can be found in the Supplementary Methods. We implemented the numerical solution algorithms using the FEniCS finite element software [Alnæs et al., 2015], and the complete simulation pipeline is openly available [Causemann, 2025].

Acknowledgments

M.E.R. acknowledges support from Stiftelsen Kristian Gerhard Jebsen via the K. G. Jebsen Centre for Brain Fluid Research and Wellcome via Award 313298/Z/24/Z (Next-generation simulation and learning in imaging-based biomedicine). M.C. and M.E.R. acknowledge support from the Research Council of Norway (RCN) via grant #324239 (EMIx). R.E. received funding from the Chan Zuckerberg Initiative DAF, an advised fund of Silicon Valley Community Foundation (grand number 2023-331840), the South-Eastern Norway Regional Health Authority (grant #2025018 and #2024079) and the Letten Foundation. Simulations were performed on the Experimental Infrastructure for Exploration of Exascale Computing (eX3), which is financially supported by the RCN under contract 270053. Figures 1B, 3A, 4A, 5A and 6A were created in Biorender.

Author contributions statement

M.C., R.E., and M.E.R. conceived and designed the project. M.C. developed the software and conducted the experiments. M.C. analyzed the results and prepared the figures. M.C. R.E. and M.E.R. wrote the manuscript. All authors edited, reviewed and approved the manuscript.

Competing interests

The authors declare no competing interests.

References

Søren Grubb. Ultrastructure of precapillary sphincters and the neurovascular unit. *Vascular Biology*, 5(1), 2023.

Thomas Misje Mathiisen, Knut Petter Lehre, Niels Christian Danbolt, and Ole Petter Ottersen. The perivascular astroglial sheath provides a complete covering of the brain microvessels: an electron microscopic 3D reconstruction. *Glia*, 58(9): 1094–1103, 2010.

N Joan Abbott, Magnus Bundgaard, and HF Cserr. Comparative physiology of the blood-brain barrier. *The blood-brain barrier in health and disease*, pages 52–72, 1986.

Grant RJ Gordon, Sean J Mulligan, and Brian A MacVicar. Astrocyte control of the cerebrovasculature. *Glia*, 55(12): 1214–1221, 2007.

Brian A MacVicar and Eric A Newman. Astrocyte regulation of blood flow in the brain. *Cold Spring Harbor perspectives in biology*, 7(5):a020388, 2015.

Jeffrey J Iliff, Minghuan Wang, Yonghong Liao, Benjamin A Plogg, Weiguo Peng, Georg A Gundersen, Helene Benveniste, G Edward Vates, Rashid Deane, Steven A Goldman, et al. A paravascular pathway facilitates CSF flow through the brain parenchyma and the clearance of interstitial solutes, including amyloid β. *Science translational medicine*, 4(147): 147ra111–147ra111, 2012.

Lulu Xie, Hongyi Kang, Qiwu Xu, Michael J Chen, Yonghong Liao, Meenakshisundaram Thiyagarajan, John O'Donnell, Daniel J Christensen, Charles Nicholson, Jeffrey J Iliff, et al. Sleep drives metabolite clearance from the adult brain. *science*, 342(6156):373–377, 2013.

Helen F Cserr and LH Ostrach. Bulk flow of interstitial fluid after intracranial injection of blue dextran 2000. *Experimental neurology*, 45(1):50–60, 1974.

T Ichimura, P A Fraser, and H F Cserr. Distribution of extracellular tracers in perivascular spaces of the rat brain. *Brain Res.*, 1991.

Humberto Mestre, Natasha Verma, Thom D Greene, LiJing A Lin, Antonio Ladron-de Guevara, Amanda M Sweeney, Guojun Liu, V Kaye Thomas, Chad A Galloway, Karen L de Mesy Bentley, et al. Periarteriolar spaces modulate cerebrospinal fluid transport into brain and demonstrate altered morphology in aging and Alzheimer's disease. *Nature communications*, 13(1): 3897, 2022.

Antoine Drieu, Siling Du, Steffen E Storck, Justin Rustenhoven, Zachary Papadopoulos, Taitea Dykstra, Fenghe Zhong, Kyungdeok Kim, Susan Blackburn, Tornike Mamuladze, et al. Parenchymal border macrophages regulate the flow dynamics of the cerebrospinal fluid. *Nature*, 611(7936):585–593, 2022.

Erlend A Nagelhus and Ole P Ottersen. Physiological roles of aquaporin-4 in brain. *Physiological reviews*, 93(4):1543–1562, 2013.

Eva K Pillai and Kristian Franze. Mechanics in the nervous system: from development to disease. *Neuron*, 112(3):342–361, 2024.

William J Tyler. The mechanobiology of brain function. *Nature Reviews Neuroscience*, 13(12):867–878, 2012.

Laura Bojarskaite, Alexandra Vallet, Daniel M Bjørnstad, Kristin M Gullestad Binder, Céline Cunen, Kjell Heuser, Miroslav Kuchta, Kent-Andre Mardal, and Rune Enger. Sleep cycle-dependent vascular dynamics in male mice and the predicted effects on perivascular cerebrospinal fluid flow and solute transport. *Nature communications*, 14(1):953, 2023.

Nicholas L Turner, Thomas Macrina, J Alexander Bae, Runzhe Yang, Alyssa M Wilson, Casey Schneider-Mizell, Kisuk Lee, Ran Lu, Jingpeng Wu, Agnes L Bodor, et al. Reconstruction of neocortex: Organelles, compartments, cells, circuits, and activity. *Cell*, 185(6):1082–1100, 2022.

Humberto Mestre, Yuki Mori, and Maiken Nedergaard. The brain's glymphatic system: current controversies. *Trends in neurosciences*, 43(7):458–466, 2020.

Yixin Hu, Teseo Schneider, Bolun Wang, Denis Zorin, and Daniele Panozzo. Fast tetrahedral meshing in the wild. *ACM Trans. Graph.*, 39(4), August 2020.

Erik N T P Bakker, Brian J Bacskai, Michal Arbel-Ornath, Roxana Aldea, Beatrice Bedussi, Alan W J Morris, Roy O Weller, and Roxana O Carare. Lymphatic clearance of the brain: Perivascular, paravascular and significance for neurodegenerative diseases. *Cell. Mol. Neurobiol.*, 36(2):181–194, March 2016.

Julian Rey and Malisa Sarntinoranont. Pulsatile flow drivers in brain parenchyma and perivascular spaces: a resistance network model study. *Fluids Barriers CNS*, 15(1):20, July 2018.

Jeffrey Tithof, Douglas H Kelley, Humberto Mestre, Maiken Nedergaard, and John H Thomas. Hydraulic resistance of periarterial spaces in the brain. *Fluids Barriers CNS*, 16(1):19, June 2019.

Antonio Ladrón-de Guevara, Jessica K Shang, Maiken Nedergaard, and Douglas H Kelley. Perivascular pumping in the mouse brain: Improved boundary conditions reconcile theory, simulation, and experiment. *Journal of theoretical biology*, 542: 111103, 2022.

Tomas Bohr, Poul G Hjorth, Sebastian C Holst, Sabina Hrabětová, Vesa Kiviniemi, Tuomas Lilius, Iben Lundgaard, Kent-Andre Mardal, Erik A Martens, Yuki Mori, U Valentin Nägerl, Charles Nicholson, Allen Tannenbaum, John H Thomas, Jeffrey Tithof, Helene Benveniste, Jeffrey J Iliff, Douglas H Kelley, and Maiken Nedergaard. The glymphatic system: Current understanding and modeling. *iScience*, 25(9):104987, September 2022.

Kimberly A S Boster, Jiatong Sun, Jessica K Shang, Douglas H Kelley, and John H Thomas. Hydraulic resistance of three-dimensional pial perivascular spaces in the brain. *Fluids Barriers CNS*, 21(1):7, January 2024.

Ingeborg G Gjerde, Miroslav Kuchta, Marie E Rognes, and Barbara Wohlmuth. Directional flow in perivascular networks: mixed finite elements for reduced-dimensional models on graphs. *J. Math. Biol.*, 89(6):60, November 2024.

Keelin Quirk, Kimberly A S Boster, Jeffrey Tithof, and Douglas H Kelley. A brain-wide solute transport model of the glymphatic system. *J. R. Soc. Interface*, 21(219):20240369, October 2024.

Eugen Solenov, Hiroyuki Watanabe, Geoffrey T Manley, and AS Verkman. Sevenfold-reduced osmotic water permeability in primary astrocyte cultures from AQP-4-deficient mice, measured by a fluorescence quenching method. *American Journal of Physiology-Cell Physiology*, 286(2):C426–C432, 2004.

Peter AR Bork, Michael Gianetto, Evan Newbold, Lauren Hablitz, Tomas Bohr, and Maiken Nedergaard. Blood osmolytes such as sugar can drive brain fluid flows in a poroelastic model. *Scientific Reports*, 14(1):29017, 2024.

Simon G Patching. Glucose transporters at the blood-brain barrier: function, regulation and gateways for drug delivery. *Molecular neurobiology*, 54(2):1046–1077, 2017.

Humberto Mestre, Jeffrey Tithof, Ting Du, Wei Song, Weiguo Peng, Amanda M Sweeney, Genaro Olveda, John H Thomas, Maiken Nedergaard, and Douglas H Kelley. Flow of cerebrospinal fluid is driven by arterial pulsations and is reduced in hypertension. *Nature communications*, 9(1):4878, 2018.

Stephanie Holstein-Rønsbo, Yiming Gan, Michael J Giannetto, Martin Kaag Rasmussen, Björn Sigurdsson, Felix Ralf Michael Beinlich, Laura Rose, Verena Untiet, Lauren M Hablitz, Douglas H Kelley, et al. Glymphatic influx and clearance are accelerated by neurovascular coupling. *Nature neuroscience*, 26(6):1042–1053, 2023.

Ravi Teja Kedarasetti, Patrick J Drew, and Francesco Costanzo. Arterial vasodilation drives convective fluid flow in the brain: a poroelastic model. *Fluids and Barriers of the CNS*, 19(1):34, 2022.

A Procès, M Luciano, Y Kalukula, L Ris, and S Gabriele. Multiscale mechanobiology in brain physiology and diseases. frontiers in cell and developmental biology, 10, 2022.

Alex Mogilner and Angelika Manhart. Intracellular fluid mechanics: Coupling cytoplasmic flow with active cytoskeletal gel. *Annual Review of Fluid Mechanics*, 50:347–370, 2018.

Peter AR Bork, Antonio Ladrón-de Guevara, Anneline H Christensen, Kaare H Jensen, Maiken Nedergaard, and Tomas Bohr. Astrocyte endfeet may theoretically act as valves to convert pressure oscillations to glymphatic flow. *Journal of the Royal Society Interface*, 20(204):20230050, 2023.

Yiming Gan, Stephanie Holstein-Rønsbo, Maiken Nedergaard, Kimberly AS Boster, John H Thomas, and Douglas H Kelley. Perivascular pumping of cerebrospinal fluid in the brain with a valve mechanism. *Journal of the Royal Society Interface*, 20 (206):20230288, 2023.

Timo Koch, Vegard Vinje, and Kent-André Mardal. Estimates of the permeability of extra-cellular pathways through the astrocyte endfoot sheath. *Fluids and Barriers of the CNS*, 20(1):1–18, 2023.

Byung-Ju Jin, Alex J Smith, and Alan S Verkman. Spatial model of convective solute transport in brain extracellular space does not support a "glymphatic" mechanism. *Journal of General Physiology*, 148(6):489–501, 2016.

Stephen B Hladky and Margery A Barrand. The glymphatic hypothesis: the theory and the evidence. *Fluids and Barriers of the CNS*, 19(1):9, 2022.

Geoffrey T Manley, Miki Fujimura, Tonghui Ma, Nobuo Noshita, Ferda Filiz, Andrew W Bollen, Pak Chan, and AS10655103 Verkman. Aquaporin-4 deletion in mice reduces brain edema after acute water intoxication and ischemic stroke. *Nature medicine*, 6(2):159–163, 2000.

Mahmood Amiry-Moghaddam, Takashi Otsuka, Patricia D Hurn, Richard J Traystman, Finn-Mogens Haug, Stanley C Froehner, Marvin E Adams, John D Neely, Peter Agre, Ole Petter Ottersen, et al. An α-syntrophin-dependent pool of AQP4 in astroglial end-feet confers bidirectional water flow between blood and brain. *Proceedings of the National Academy of Sciences*, 100(4): 2106–2111, 2003.

Marios C Papadopoulos, Geoffrey T Manley, Sanjeev Krishna, and AS Verkman. Aquaporin-4 facilitates reabsorption of excess fluid in vasogenic brain edema. *The FASEB journal*, 18(11):1291–1293, 2004.

Jan Tønnesen, VVG Krishna Inavalli, and U Valentin Nägerl. Super-resolution imaging of the extracellular space in living brain tissue. *Cell*, 172(5):1108–1121, 2018.

Jan Tønnesen, Sabina Hrabětová, and Federico N Soria. Local diffusion in the extracellular space of the brain. *Neurobiology of Disease*, 177:105981, 2023.

Ravi Teja Kedarasetti, Kevin L Turner, Christina Echagarruga, Bruce J Gluckman, Patrick J Drew, and Francesco Costanzo. Functional hyperemia drives fluid exchange in the paravascular space. *Fluids and Barriers of the CNS*, 17:1–25, 2020.

Emad Moeendarbary, Léo Valon, Marco Fritzsche, Andrew R. Harris, Dale A. Moulding, Adrian J. Thrasher, Eleanor Stride, L. Mahadevan, and Guillaume T. Charras. The cytoplasm of living cells behaves as a poroelastic material. *Nature Materials*, 12(3), March 2013. ISSN 1476-1122. doi: 10.1038/nmat3517.

Mohammad Hadi Esteki, Andrea Malandrino, Ali Akbar Alemrajabi, Graham K. Sheridan, Guillaume Charras, and Emad Moeendarbary. Poroelastic osmoregulation of living cell volume. *iScience*, 24(12), December 2021. ISSN 2589-0042. doi: 10.1016/j.isci.2021.103482. URL https://www.sciencedirect.com/science/article/pii/S258900422101453X.

Maurice A Biot. General theory of three-dimensional consolidation. *Journal of applied physics*, 12(2):155–164, 1941.

Yun-Bi Lu, Kristian Franze, Gerald Seifert, Christian Steinhäuser, Frank Kirchhoff, Hartwig Wolburg, Jochen Guck, Paul Janmey, Er-Qing Wei, Josef Käs, and Andreas Reichenbach. Viscoelastic properties of individual glial cells and neurons in the CNS. *Proceedings of the National Academy of Sciences*, 103(47):17759–17764, November 2006. doi: 10.1073/pnas.0606150103. URL https://www.pnas.org/doi/full/10.1073/pnas.0606150103. Publisher: Proceedings of the National Academy of Sciences.

I.G. Bloomfield, I.H. Johnston, and L.E. Bilston. Effects of Proteins, Blood Cells and Glucose on the Viscosity of Cerebrospinal Fluid. *Pediatric Neurosurgery*, 28(5):246–251, 1998. ISSN 1016-2291, 1423-0305. doi: 10.1159/000028659. URL https://www.karger.com/Article/FullText/28659.

Peng Wang and William L. Olbricht. Fluid mechanics in the perivascular space. *Journal of Theoretical Biology*, 274(1): 52–57, April 2011. ISSN 0022-5193. doi: 10.1016/j.jtbi.2011.01.014. URL https://www.sciencedirect.com/science/article/pii/S0022519311000269.

Silvia Budday, Timothy C Ovaert, Gerhard A Holzapfel, Paul Steinmann, and Ellen Kuhl. Fifty shades of brain: a review on the mechanical testing and modeling of brain tissue. *Archives of Computational Methods in Engineering*, 27:1187–1230, 2020.

Karl Erik Holter, Benjamin Kehlet, Anna Devor, Terrence J Sejnowski, Anders M Dale, Stig W Omholt, Ole Petter Ottersen, Erlend Arnulf Nagelhus, Kent-André Mardal, and Klas H Pettersen. Interstitial solute transport in 3D reconstructed neuropil occurs by diffusion rather than bulk flow. *Proceedings of the National Academy of Sciences*, 114(37):9894–9899, 2017.

Qingguo Hong and Johannes Kraus. Parameter-robust stability of classical three-field formulation of Biot's consolidation model. *arXiv preprint arXiv:1706.00724*, 2017.

Xiaozhe Hu, Carmen Rodrigo, Francisco J Gaspar, and Ludmil T Zikatanov. A nonconforming finite element method for the Biot's consolidation model in poroelasticity. *Journal of Computational and Applied Mathematics*, 310:143–154, 2017.

Martin Alnæs, Jan Blechta, Johan Hake, August Johansson, Benjamin Kehlet, Anders Logg, Chris Richardson, Johannes Ring, Marie E Rognes, and Garth N Wells. The FEniCS project version 1.5. *Archive of numerical software*, 3(100), 2015.

Marius Causemann. Software and data for "stretch and flow at the gliovascular interface: high-fidelity modelling of the mechanics of astrocyte endfeet", April 2025. URL https://doi.org/10.5281/zenodo.15303023.

Michel Crouzeix and P-A Raviart. Conforming and nonconforming finite element methods for solving the stationary Stokes equations I. *Revue française d'automatique informatique recherche opérationnelle. Mathématique*, 7(R3):33–75, 1973.

Pierre-Arnaud Raviart and Jean-Marie Thomas. A mixed finite element method for 2nd order elliptic problems, mathematical aspects of finite element methods (proc. conf., consiglio naz. delle ricerche (cnr), rome, 1975), vol. 606 of lecture notes in mathematics, 1977.

Jean-Claude. Nédélec. Mixed finite elements in $\mathbb{R}^3$. *Numerische Mathematik*, 35:315–341, 1980.

Peter Hansbo and Mats G Larson. Discontinuous Galerkin and the Crouzeix–Raviart element: application to elasticity. *ESAIM: Mathematical Modelling and Numerical Analysis*, 37(1):63–72, 2003.

A Supplementary methods

These sections provide a complete description of the mathematical model and numerical approximations employed.

A.1 Three-field formulation of the cell-by-cell dual poroelasticity model

We restate the system of coupled poroelasticity equations given by (1) with the fluid flux $\mathbf{q} = -\frac{\kappa}{\mu_F}\nabla p$ as an additional unknown. The equations then read: find the displacement $\mathbf{d} : \Omega_i \cup \Omega_e \to \mathbb{R}$, the fluid pressure $p : \Omega_i \cup \Omega_e \to \mathbb{R}$, and the fluid flux $\mathbf{q} : \Omega_i \cup \Omega_e \to \mathbb{R}$ such that

$$\begin{aligned} -\mathbf{div}\,(2\mu_S \boldsymbol{\varepsilon}(\mathbf{d}) + \lambda \operatorname{div} \mathbf{d}\mathbf{I} - \alpha p \mathbf{I}) &= 0, \\ \mathbf{q} + \frac{\kappa}{\mu_F}\nabla p &= 0, \\ s\partial_t p + \alpha \partial_t \operatorname{div} \mathbf{d} + \operatorname{div} \mathbf{q} &= 0, \end{aligned} \tag{8}$$

all over Ω_i, Ω_e. The interface conditions (2) and (3) on the cell membrane $\Gamma = \overline{\Omega_i} \cap \overline{\Omega_e}$ read as

$$\mathbf{q}\cdot\mathbf{n} = L_p\left(\llbracket p \rrbracket + p_{\text{osm}}\right), \quad \llbracket \mathbf{q}\cdot\mathbf{n} \rrbracket = 0, \quad \llbracket \mathbf{d} \rrbracket = 0, \quad \llbracket (2\mu_S \boldsymbol{\varepsilon}(\mathbf{d}) + \lambda \operatorname{div} \mathbf{d}\mathbf{I} - \alpha p \mathbf{I})\cdot\mathbf{n} \rrbracket = 0, \tag{9}$$

where the jump $\llbracket \cdot \rrbracket$ denotes the difference over Γ. The complete set of dynamic boundary conditions (as summarized by Table 2) are as follows, for $t > 0$.

(i) On the inner boundary Γ_{VW}, we set:

$$\begin{aligned} \mathbf{d}(t) &= \mathbf{d}_{\text{VW}}(t) \equiv A \sin(2\pi f t)\mathbf{r}, \\ \mathbf{q}(t)\cdot\mathbf{n} &= 0, \end{aligned}$$

where A is the amplitude and f the frequency of the vessel wall motion, and $\mathbf{r}$ denotes the unit-length radial direction from the vessel centerline.

(ii) On the axial boundaries of the geometry: $\Gamma_{\text{axial}} \equiv \Gamma_{\text{ECS-axial}} \cup \Gamma_{\text{EF-axial}} \cup \Gamma_{\text{PVS-A}} \cup \Gamma_{\text{PVS-B}}$, we impose no flow:

$$\mathbf{q}(t)\cdot\mathbf{n} = 0, \tag{10}$$

except in the (open) PVS model variation with minimal PVS pathway resistance where we replace (10) on $\Gamma_{\text{PVS-B}}$ by instead imposing $p = 0$.

(iii) Also on Γ_{axial}, with the vessel centerline coinciding with the y-direction of the coordinate system, we restrict axial displacement and allow free radial movement by the following conditions

$$\mathbf{d}(t)\cdot\mathbf{e}_y = 0, \qquad \mathbf{e}_m \cdot \boldsymbol{\sigma}(t)\cdot\mathbf{n} = 0 \quad m \in \{x, z\},$$

where the poroelastic stress tensor $\boldsymbol{\sigma} \equiv 2\mu_S \boldsymbol{\varepsilon}(\mathbf{d}) + \lambda \operatorname{div} \mathbf{d}\mathbf{I} - \alpha p \mathbf{I}$, and $\mathbf{e}_x$, $\mathbf{e}_y$ and $\mathbf{e}_z$ are the unit vectors in the direction of each coordinate axis.

(iv) Assuming no displacement in the far field distance $l_{\text{far}} > 0$, we use a Robin boundary condition on the radial boundaries $\Gamma_{\text{radial}} \equiv \Gamma_{\text{EF-radial}} \cup \Gamma_{\text{ECS-radial}}$, emulating the elastic response of the surrounding tissue:

$$\boldsymbol{\sigma}(t)\cdot\mathbf{n} = \frac{E_{\text{far}}}{l_{\text{far}}}\mathbf{d}(t),$$

where E_{far} is the elastic Young modulus of the surrounding tissue.

(v) Additionally on Γ_{radial}, we allow fluid outflow across both the endfeet and the ECS outer boundaries, assuming a (homogenized) permeability κ_{far} and a far field pressure at a distance l_{far}, resulting in the condition:

$$\mathbf{q}(t)\cdot\mathbf{n} = \frac{\kappa_{\text{far}}}{\mu_F l_{\text{far}}}\left(p(t) - p_{\text{far}}\right).$$

A.2 Semi-discrete variational formulation of the three-field cell-by-cell dual poroelasticity model

We introduce the following spaces for the displacements and fluxes, respectively, incorporating the essential boundary conditions (in the sense of traces) as appropriate:

$$\begin{aligned} \mathbf{V_g} &= \{\mathbf{d} \in H^1(\Omega;\mathbb{R}^3) \,:\, \mathbf{d}|_{\Gamma_{\mathrm{VM}}} = \mathbf{g} \text{ and } \mathbf{d}\cdot\mathbf{e}_y|_{\Gamma_{\mathrm{axial}}} = 0\}, \\ \mathbf{W} &= \{\mathbf{q} \in H(\mathrm{div},\Omega) \,:\, \mathbf{q}\cdot\mathbf{n}|_{\Gamma_{\mathrm{VW}}\cup\Gamma_{\mathrm{axial}}} = 0\}. \end{aligned} \tag{11}$$

In (11), $H^1(\Omega;\mathbb{R}^3)$ and $H(\mathrm{div},\Omega)$ are the standard Sobolov spaces of square-integrable vector-valued functions with square-integrable gradient components and divergence, respectively. We denote the $L^2(\Omega)$-inner product as

$$(a,b)_\Omega \equiv \int_\Omega a\cdot b\,\mathrm{d}\boldsymbol{x} \tag{12}$$

and omit the subscript Ω when $\Omega = \Omega_i \cup \Omega_e$.

After time discretization with an implicit Euler method, the time-dependent problem, equipped with the initial conditions

$$\mathbf{d}^0 = \mathbf{0} \quad \text{and} \quad p^0 = 0,$$

simplifies to the following sequence of stationary, semi-discrete variational problems: for $n = 1,2,3,\ldots$, with time step size $\tau^n \equiv t^n - t^{n-1} > 0$, find $\mathbf{d}^n \in \mathbf{V}_{\mathbf{d}_{\mathrm{VW}}(t^n)}$, $\mathbf{q}^n \in \mathbf{W}$ and $p^n \in L^2(\Omega)$ satisfying

$$(2\mu_S\boldsymbol{\varepsilon}(\mathbf{d}^n),\boldsymbol{\varepsilon}(\mathbf{v})) + \lambda(\mathrm{div}\,\mathbf{d}^n,\mathrm{div}\,\mathbf{v}) - (\alpha p^n,\mathrm{div}\,\mathbf{v}) + r_d(\mathbf{d}^n,\mathbf{v}) = 0 \qquad \forall\,\mathbf{v}\in\mathbf{V_0} \tag{13a}$$

$$(K^{-1}\mathbf{q}^n,\mathbf{w}) - (p^n,\mathrm{div}\,\mathbf{w}) + (L_p^{-1}\mathbf{q}^n\cdot\mathbf{n},\mathbf{w}\cdot\mathbf{n})_\Gamma + r_q(\mathbf{q}^n,\mathbf{w}) = (p_{\mathrm{osm}},\mathbf{w}\cdot\mathbf{n})_\Gamma \qquad \forall\,\mathbf{w}\in\mathbf{W} \tag{13b}$$

$$(\alpha\tau^{-1}\,\mathrm{div}\,\mathbf{d}^n,\phi) + (\mathrm{div}\,\mathbf{q}^n,\phi) + (s\tau^{-1}p^n,\phi) = (\alpha\tau^{-1}\,\mathrm{div}\,\mathbf{d}^{n-1} + s\tau^{-1}p^{n-1},\phi) \qquad \forall\,\phi\in L^2(\Omega) \tag{13c}$$

The hydraulic conductivity K is defined by $K = \frac{\kappa}{\mu_F}$. With the far field distance l_{far}, the Young modulus E_{far} and hydraulic conductivity K_{far} of the surrounding tissue, the contributions from the Robin boundary conditions are as follows:

$$\begin{aligned} r_d(\mathbf{d},\mathbf{v}) &= (\frac{E_{\mathrm{far}}}{l_{\mathrm{far}}}\mathbf{d},\mathbf{v})_{\Gamma_{\mathrm{radial}}}, \\ r_q(\mathbf{q},\mathbf{w}) &= (K_{\mathrm{far}}^{-1}l_{\mathrm{far}}\mathbf{q}\cdot\mathbf{n},\mathbf{w}\cdot\mathbf{n})_{\Gamma_{\mathrm{radial}}}. \end{aligned}$$

Note that the interface term $(L_p^{-1}\mathbf{q}^n\cdot\mathbf{n},\mathbf{w}\cdot\mathbf{n})_\Gamma$ and the Robin term $r_q(\cdot,\cdot)$ in (13b) stems from integration by parts and insertion of the interface flux condition (2) in the following manner:

$$\begin{aligned} &\int_{\Omega_i\cup\Omega_e} K^{-1}\mathbf{q}^n\cdot\mathbf{w} + \nabla p^n\cdot\mathbf{w}\,\mathrm{d}\boldsymbol{x} \\ &= \int_{\Omega_i\cup\Omega_e} K^{-1}\mathbf{q}^n\cdot\mathbf{w}\,\mathrm{d}\boldsymbol{x} - \int_{\Omega_i\cup\Omega_e} p^n\,\mathrm{div}\,\mathbf{w}\,\mathrm{d}\boldsymbol{x} + \int_\Gamma p^n|_{\Omega_i}\mathbf{w}\cdot\mathbf{n}\,\mathrm{d}s - \int_\Gamma p^n|_{\Omega_e}\mathbf{w}\cdot\mathbf{n}\,\mathrm{d}s + \int_{\Gamma_{\mathrm{radial}}} p^n\mathbf{w}\cdot\mathbf{n}\,\mathrm{d}s \\ &= (K^{-1}\mathbf{q}^n,\mathbf{w}) - (p^n,\mathrm{div}\,\mathbf{w}) + (\llbracket p^n\rrbracket,\mathbf{w}\cdot\mathbf{n})_\Gamma + (K_{\mathrm{far}}^{-1}l_{\mathrm{far}}\mathbf{q}^n\cdot\mathbf{n},\mathbf{w}\cdot\mathbf{n})_{\Gamma_{\mathrm{radial}}} \\ &\qquad = (K^{-1}\mathbf{q}^n,\mathbf{w}) - (p^n,\mathrm{div}\,\mathbf{w}) + (L_p^{-1}\mathbf{q}^n\cdot\mathbf{n} - p_{\mathrm{osm}},\mathbf{w}\cdot\mathbf{n})_\Gamma + r(\mathbf{q}^n,\mathbf{w}) \end{aligned} \tag{14}$$

for all $\mathbf{w}\in\mathbf{W}$.

A.3 Fully discrete approximation and numerical solution of the cell-by-cell dual poroelasticity model

We consider a mesh $\mathcal{T} = \{E\}$ of $\Omega = \Omega_i \cup \Omega_e$, consisting of tetrahedral mesh cells E, and conforming to the domains Ω_i and Ω_e and to the cell membrane Γ. We denote the restriction of $\mathcal{T}$ to Ω_i and Ω_e by $\mathcal{T}_i$ and $\mathcal{T}_e$, respectively. The collection of all interior facets (i.e. triangular faces of the tetrahedral mesh cells) in $\mathcal{T}_i$ and $\mathcal{T}_e$ are denoted by $\mathcal{F}_{i,i}$ and $\mathcal{F}_{i,e}$, respectively. We define the union of facets interior both to $\mathcal{T}_i$ and $\mathcal{T}_e$ as $\mathcal{F}_i = \mathcal{F}_{i,i} \cup \mathcal{F}_{i,e}$. Moreover, we denote the exterior facets associated with the boundary parts Γ_{VW}, $\Gamma_{\mathrm{PVS-A}}$, $\Gamma_{\mathrm{PVS-B}}$, $\Gamma_{\mathrm{EF-axial}}$, $\Gamma_{\mathrm{EF-radial}}$, $\Gamma_{\mathrm{ECS-axial}}$, Γ_{axial} and $\Gamma_{\mathrm{ECS-radial}}$ with $\mathcal{F}_{\mathrm{VW}}$, $\mathcal{F}_{\mathrm{PVS-A}}$, $\mathcal{F}_{\mathrm{PVS-B}}$, $\mathcal{F}_{\mathrm{EF-axial}}$, $\mathcal{F}_{\mathrm{EF-radial}}$, $\mathcal{F}_{\mathrm{ECS-axial}}$, $\mathcal{F}_{\mathrm{axial}}$ and $\mathcal{F}_{\mathrm{ECS-radial}}$, respectively.

To solve (13) numerically, we utilize a non-conforming discontinuous Galerkin discretization, with a formulation proposed by Hu et al. [2017] in the case of a single poroelastic domain. In particular, we use Crouzeix–Raviart elements for the displacements $\mathbf{d}$ (which are only continuous at the facet barycenter and thus are not conforming in H^1), the lowest order Raviart–Thomas-Nédélec elements for the Darcy velocity $\mathbf{q}$ and piecewise constants for the fluid pressure p, all defined relative to the mesh $\mathcal{T}$. This method is locally mass conservative and locking-free, and its comparably low number of degrees of

freedom per mesh cell makes it suitable for high-resolution meshes of complex geometries. More precisely, the non-conforming Crouzeix-Raviart space is defined as [Crouzeix and Raviart, 1973]:

$$\mathbf{V}_{\mathbf{g},h} = \{\mathbf{d}_h \in L^2(\Omega;\mathbb{R}^3) : \mathbf{d}_h|_E \in \mathcal{P}^1(E)^3 \quad \forall E \in \mathcal{T}; \\ \int_e [\![\mathbf{d}_h]\!] = 0 \quad \forall e \in \mathcal{F}_i; \int_e [\![\mathbf{d}_h - \mathbf{g}]\!] = 0 \quad \forall e \in \mathcal{F}_{\mathrm{VW}}; \int_e [\![\mathbf{d}_h \cdot \mathbf{e}_y]\!] = 0 \quad \forall e \in \mathcal{F}_{\mathrm{axial}}\}, \tag{15}$$

where $\mathcal{P}^1(E)$ denotes the space of linear polynomials defined over the tetrahedra E. Note that the continuity condition $\int_e [\![\mathbf{d}_h]\!] = 0$ for all $e \in \mathcal{F}_i$ is equivalent to continuity at the barycenter of each facet. Further, we set

$$\mathbf{W}_h = \{\mathbf{q} \in H(\mathrm{div},\Omega) : \mathbf{q}|_E \in \mathrm{RT}(E), \quad E \in \mathcal{T}; \quad \mathbf{q}\cdot\mathbf{n}|_{\Gamma_{\mathrm{VW}}\cup\Gamma_{\mathrm{axial}}} = 0\}, \tag{16}$$

where RT denotes the lowest order Raviart-Thomas-Nédélec elements [Raviart and Thomas, 1977, Nédélec, 1980]. Finally, we use the space of piecewise constant functions on each element to approximate the fluid pressure and denote it by Q_h.

In order to ensure the coercivity of the bilinear form

$$a(\mathbf{d},\mathbf{v}) = (2\mu_S \boldsymbol{\varepsilon}(\mathbf{d}), \boldsymbol{\varepsilon}(\mathbf{v})) + \lambda(\mathrm{div}\,\mathbf{d}, \mathrm{div}\,\mathbf{v}), \quad \forall \mathbf{d},\mathbf{v} \in \mathbf{V}_{0,h}, \tag{17}$$

in the discrete case for the non-conforming Crouzeix-Raviart elements, we include a standard stabilization term [Hansbo and Larson, 2003], which leads to the following modified form:

$$a_h(\mathbf{d},\mathbf{v}) = a(\mathbf{d},\mathbf{v}) + 2\mu_s\eta \sum_{e\in\mathcal{F}_i} h_e^{-1} [\![\mathbf{d}]\!][\![\mathbf{v}]\!] \quad \forall \mathbf{d},\mathbf{v} \in \mathbf{V}_{0,h}. \tag{18}$$

In (18), h_e denotes the average cell diameter of the cells associated with the edge e and $\eta > 0$ is a penalty parameter. (We choose $\eta = 1$.) As shown by Hansbo and Larson [2003] for the equations of linear elasticity, the stabilization ensures positive definiteness of the bilinear form $a_h(\cdot,\cdot)$ and optimal approximation properties of the scheme.

In summary, the fully discrete formulation of (13) with the initial conditions

$$\mathbf{d}_h^0 = \mathbf{d}(0) \quad \text{and} \quad p_h^0 = p(0) \tag{19}$$

then reads: for $n = 1,2,3,\ldots$, find $\mathbf{d}_h^n \in \mathbf{V}_{\mathbf{d}_{\mathrm{VW}}(t^n),h}$, $\mathbf{q}_h^n \in \mathbf{W}_h$ and $p_h^n \in Q_h$, such that:

$$\begin{aligned} a_h(\mathbf{d}_h^n,\mathbf{v}) - (\alpha p_h^n, \mathrm{div}\,\mathbf{v}) + r_d(\mathbf{d}_h^n,\mathbf{v}) &= 0 && \forall \mathbf{v} \in \mathbf{V}_{0,h} \\ (K^{-1}\mathbf{q}_h^n,\mathbf{w}) - (p_h^n, \mathrm{div}\,\mathbf{w}) + (L_p^{-1}\mathbf{q}_h^n\cdot\mathbf{n}, \mathbf{w}\cdot\mathbf{n})_\Gamma + r_q(\mathbf{q}_h^n,\mathbf{w}) &= (p_{\mathrm{osm}}, \mathbf{w}\cdot\mathbf{n})_\Gamma && \forall \mathbf{w} \in \mathbf{W}_h \\ (\alpha\tau^{-1}\,\mathrm{div}\,\mathbf{d}_h^n,\phi) + (\mathrm{div}\,\mathbf{q}_h^n,\phi) + (s\tau^{-1}p_h^n,\phi) &= (\alpha\tau^{-1}\,\mathrm{div}\,\mathbf{d}_h^{n-1} + s\tau^{-1}p_h^{n-1},\phi) && \forall \phi \in Q_h. \end{aligned} \tag{20}$$

Stability and optimal order a-priori error estimates of this scheme have been shown by Hu et al. [2017] for the single domain case. Our numerical results, in part included in the Numerical verification section below, indicate that such also hold for the coupled poroelastic problem considered here.

A.4 Numerical verification

We assess the numerical accuracy and convergence of our simulation results by performing experiments with different spatial resolutions. Specifically, we generate a second mesh with roughly twice the number of computational mesh vertices (standard mesh: 158,239 vs. refined: 333,034) and cells (standard: 798,272 vs. refined: 1,704,408), solve the baseline model on both meshes, and compare the results across meshes for a set of key quantities of interest (Figure 7). Finding only minor differences between the two meshes (all relative differences below 10 %, most below 5 %), we conclude that the standard resolution mesh offers sufficient accuracy for our simulations.

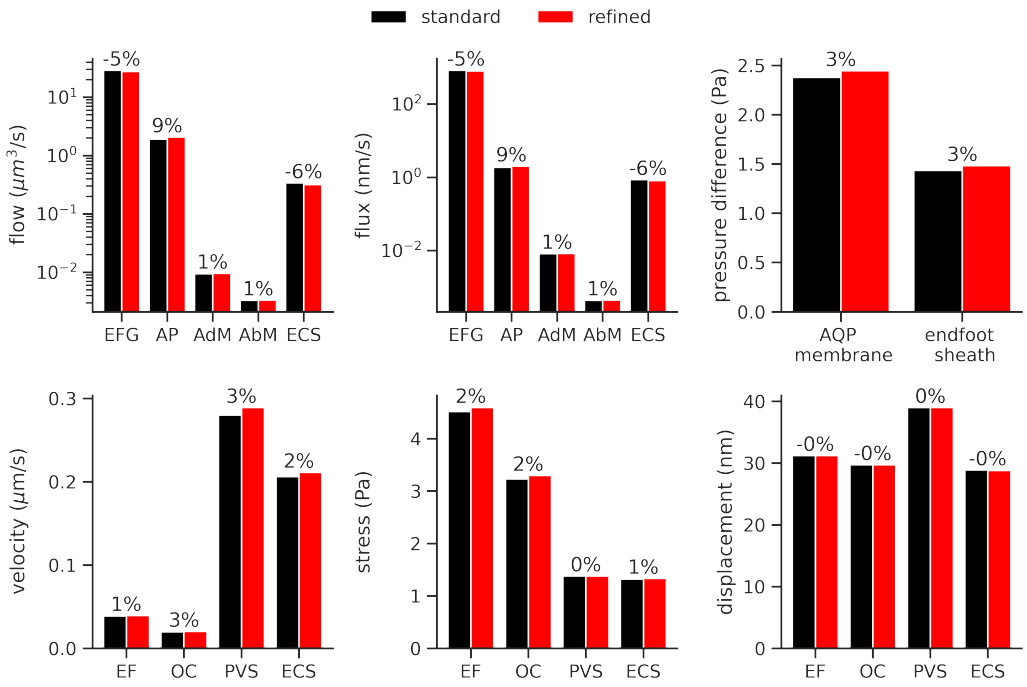

Figure 7. Verification of computational results. Numerical verification by comparing key simulated quantities of interest on the standard and a refined mesh with roughly double the number of vertices (258 776 (standard mesh) vs. 494 811 (refined)) and cells (1 425 200 (standard) vs. 2 711 209 (refined)). The percentage above each bar pair (A–F) denotes the relative difference between the quantities computed on the different meshes, revealing only minor differences (9% maximum).